MICROSTRUCTURE AND STRENGTHENING MECHANISMS OF HIGHLY TEXTURED Cu/Ni MULTILAYERS

A Thesis

by

YUE LIU

Submitted to the Office of Graduate Studies of
Texas A&M University
in partial fulfillment of the requirements for the degree of

MASTER OF SCIENCE

August 2010

Major Subject: Mechanical Engineering

MICROSTRUCTURE AND STRENGTHENING MECHANISMS OF HIGHLY TEXTURED Cu/Ni MULTILAYERS

A Thesis

by

YUE LIU

Submitted to the Office of Graduate Studies of
Texas A&M University
in partial fulfillment of the requirements for the degree of

MASTER OF SCIENCE

Approved by:

Chair of Committee	Xinghang Zhang
Committee Members	Hong Liang
	Haiyan Wang
Head of Department	Dennis O'Neal

August 2010

Major Subject: Mechanical Engineering

ABSTRACT

Microstructure and Strengthening Mechanisms of Highly Textured Cu / Ni Multilayers.

(August 2010)

Yue Liu, B.S., Fudan University, Shanghai, China P.R.

Chair of Advisory Committee: Dr. Xinghang Zhang

In this thesis, I planned to fabricate Cu/Ni metallic multilayers with equal layer thicknesses on different substrates by using magnetic sputtering technique. My objective was to characterize the texture, structure and hardness, in order to study strengthening mechanisms and nanotwins in the Cu/Ni multilayers.

Sputtered, highly textured (111) and (100) Cu/Ni multilayers with individual layer thickness, h, vary from 1 to 200 nm. At greater h, X-ray diffraction (XRD) patterns of Cu and Ni (100 or 111) peaks are clearly separated indicating that the interface between Cu and Ni is semi-coherent. When h decreases to 5 nm or less, XRD spectra show significant peak distortions due to coherency stress. High resolution microscopy studies confirm the coexistence of nanotwins and coherent layer interfaces in highly (111) textured Cu/Ni mutilayers. Nanoscale twins can be formed in Cu at all h and in Ni at smaller h. Multilayer hardnesses increase with decreasing h, approach maxima at h of 2.5-5 nm, and show softening thereafter. A detail comparison between (111) and (100) textured Cu/Ni is made in both microstructure and strengthening.

In this thesis, the possible mechanisms to form high density growth twins in Ni are discussed. Furthermore, the influences of both coherent layer interfaces and twin interfaces on strengthening mechanisms are discussed.

to my parents

ACKOWLEDGEMENTS

First and foremost I would like to thank my advisor, Prof. Xinghang Zhang, for providing this great research opportunity. His consistent encouragement and financial support through this research made this work possible. His insightful discussion, patience in explaining science, critical thinking, and direction of the project have been invaluable.

I would like to thank the other members of my committee, Prof. Haiyan Wang and Prof. Hong Liang, for their guidance and suggestions that helped shape this thesis.

I would like to thank my colleagues and friends, N. Li, O. Anderoglu, E.G. Fu, S. Rios, D. Bufford, B. Ham, N. Jetta, J. Gonzalez, K. Yu, C. Sun, F. Gao, Z. Bi, J. Lee, I. Kim, C. Cai, Y. Zhu, L. Chen, Q. Su and A. Chen. I appreciate their friendship and support during this period. The technical and administrative staff in the Department of Mechanical Engineering and Texas A&M University deserve mention.

I would like to express my deepest gratitude to my parents and Chu Wang. Without their understanding and support, I would not have made it through.

TABLE OF CONTENTS

LIST OF FIGURES

FIGURE Page

FIGURE Page

LIST OF TABLES

CHAPTER I

INTRODUCTION

1.1 Crystalline structure in thin film

A crystalline solid has long range order. Its atoms are typically arranged in an orderly repeating pattern extending in all three dimensions. In contrast, an amorphous solid, does not have long-range order, but may have short range and sometimes medium range orders. In this thesis we will only deal with crystalline metals in multilayer format.

In crystalline metals, body centered cubic (BCC), face centered cubic (FCC) and hexagonal closely packed (HCP) structures are the most common structures that are extensively studied. As shown in Figure 1.1, a single crystal has no grain boundaries and the properties of the material, such as electrical conductivity and magnetic properties (magnetization) could be maximized. Although single crystal is desirable in numerous applications, polycrystalline metals are encountered more frequently. Polycrystalline metals have grain boundaries, various grain size and distribution, and the orientation can vary from random to strong texture.

This thesis follows the style of Journal of Applied Physics.

Single crystal like metal films can be fabricated in a variety of ways. These films can be grown through epitaxial process, and as a result can possess single crystal or highly textured orientation. Low angle grain boundaries might exist in highly textured films, but the misorientation is much less. The word "epitaxial" means extended single crystal film formation on top of a crystalline substrate. During epitaxial growth, the deposited film takes on a lattice structure and orientation identical to that of the substrate. An epitaxial film can also be referred as a single-crystal like film. If a film is deposited on a substrate of the same composition (such as Si), the process is called homoepitaxy; otherwise it is called heteroepitaxy. Misfit dislocations typically exist in heteroepitaxial films due to the difference in lattice parameters. Furthermore there is very often an elastic modulus difference.

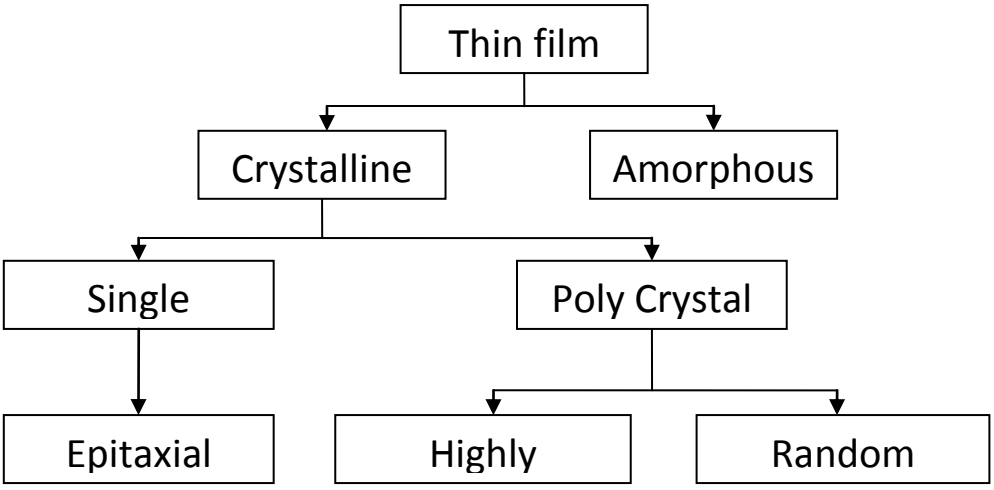

Figure 1.1 Classifications of materials.

X-ray diffraction (XRD) technique has been commonly used to examine the crystal structure and textures. Since the difference between highly textured and epitaxial

films can be subtle, both in-plane and out-of-plane XRD measurements have to be performed. Furthermore plane-view and cross-sectional transmission electron microscopy (TEM) experiments are extensively used to characterize the details and epxitaxial relation between films and substrates.

1.2 Thin film deposition techniques

A variety of thin film deposition techniques are applied in thin film fabrication. Besides some techniques with chemical reaction process, physical vapor deposition (PVD) and chemical vapor deposition (CVD) are the two main categories of techniques for thin film depositions.

1.2.1 Physical vapor deposition (PVD)

PVD technique can deposit thin films by condensing vapor (from source) to the substrate. Typical PVD technique induces vapors from source by either evaporation or ion bombardment (sputtering). Some typical PVD techniques are provided in Figure 1.2.

a. Thermal evaporation

This is a PVD technique to transfer atoms from a heated source to a substrate, where film formation and growth proceed automatically. It is an equilibrium process with no atom bombardment on the substrates. The deposition rate and composition is dominated by evaporation flux φ.

b. Electron-beam (e-beam) evaporation

Comparing with thermal evaporation technique, the only difference of e-beam evaporation technique is the heating source. In this case the target material is heated by electron beam in high vacuum. This could avoid contamination from crucible and support materials in thermal evaporation.

c. Molecular beam epitaxy (MBE)

MBE is a highly advanced e-beam technique used to deposit high quality single crystal films. MBE takes place in ultra high vacuum (10^{-10} torr). Very slow deposition rate of MBE allows the films to grow epitaxially. RHEED (Reflection high energy electron diffraction) is often used for monitoring the growth of the layers during MBE operation.

d. Pulsed laser deposition (PLD)

Pulsed laser deposition (PLD) is a PVD technique where a high power pulsed laser beam strikes a target material inside a high vacuum chamber. The material is vaporized from the target and then deposited on a substrate. It is a non-equilibrium process due to the high energy of deposition atoms (~10ev) which is provided by high energy laser beam.

e. Magnetron sputtering (DC, RF)

Magnetron sputtering is a process where atoms are ejected from a solid target material due to the bombardment of the target by energetic ions. Direct current (DC) or Radio frequency (RF) and magnetic field (from magnetron) are applied to drive the atoms from a target to a substrate, and then bombard the substrate with high kinetic

energy (~ 1 kev). Thus, it is a non-equilibrium deposition process. Comparing with electrodepositions, magnetron sputtering has lower deposition rate and better film quality. However, magnetron sputtering has much higher deposition rate compare with other PVD techniques, such as MBE and PLD. It is commonly used for high quality thin film deposition.

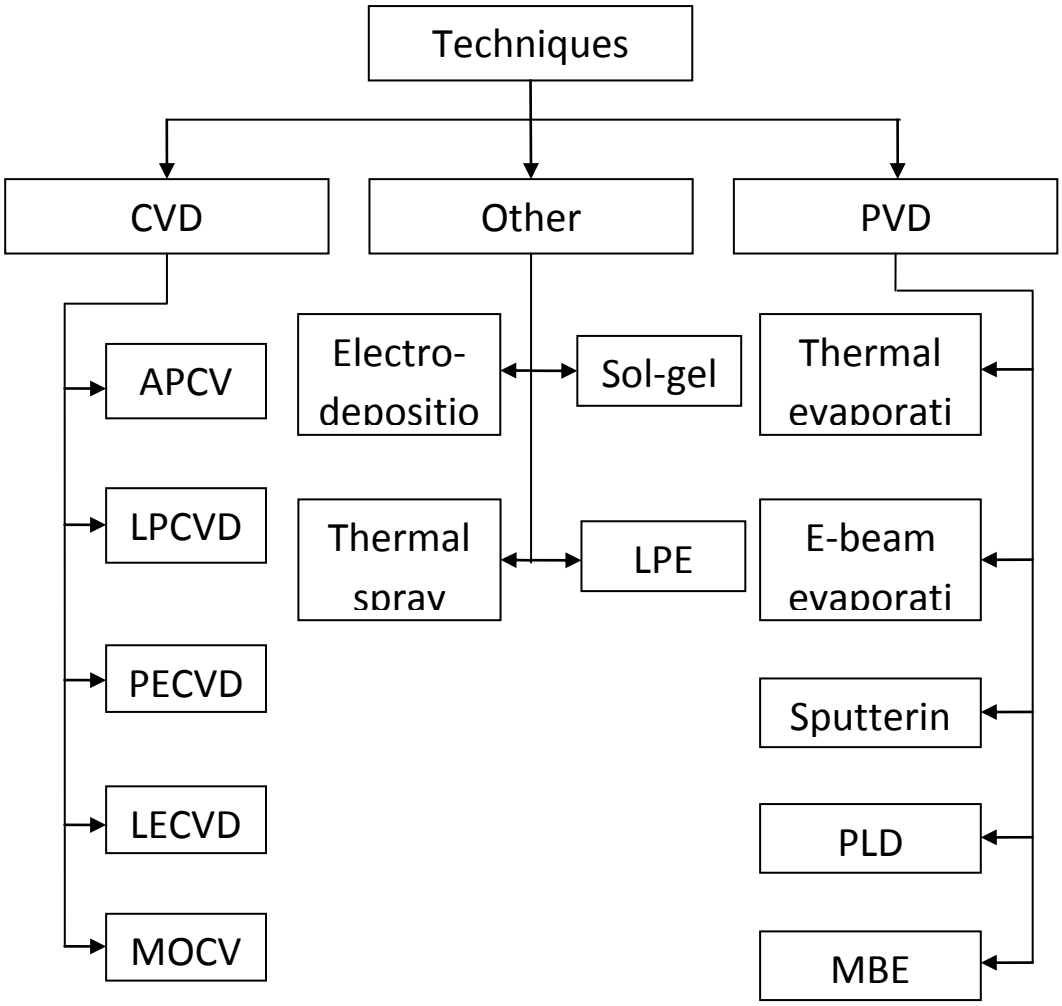

Figure 1.2 Thin film deposition techniques.

During sputtering deposition, it follows three major processes. At first, Argon ions are accelerated by across cathode sheath; High kinetic energy cascade ions collide and penetrate to the target; Recoiled target atoms are ejected and then bombard a substrate by DC, RF or magenetic field. Sputter yield, is defined to identify the average number of atoms ejected from the target per incident ion. Numbers of parameters, including projectile kinetic energy, target surface binding energy, projectile identity (Z), incidence angle, and sputtered atom angular distribution are some major factors to determine the sputter yield. Based on this, argon pressure and deposition power are main concerns to determine the deposition rate. The distance between substrate and target is another straightforward factor to affect the deposition rate.

1.2.2 Chemical vapor deposition (CVD)

Chemical Vapor Deposition (CVD) is chemical process used to produce high-purity solid materials. The process is often used in the semiconductor industry to produce thin films. In a typical CVD process, reactants are transported by forced convection to the deposition region at first; the reactants are transported by diffusion from the main gas stream through the boundary layer to the substrate surface; the reactants are adsorbed on the surface; chemical deposition or reaction at the surface; deposition of byproducts from the surface; the other waste byproducts are transported by diffusion and forced convection. As shown in Figure 1.2, there are some specific CVD techniques and principles.

Atmospheric CVD (APCVD) is a basic CVD technique. Atmospheric pressure and high temperature is applied in this technique to increase the deposition rate. Low pressure CVD (LPCVD) is a CVD technique that processes at low pressures, and lower temperature. Reduced pressures tend to reduce unwanted gas-phase reactions and improve film uniformity. Plasma enhanced CVD (PECVD) is a CVD technique that utilizes plasma to enhance chemical reaction rate of the precursors. It allows deposition at lower temperatures, which is significant in the manufacture of semiconductors. Atomic Layer CVD (ALCVD), also called atomic layer deposition (ALD), or Atomic layer epitaxy (ALE), is a specialized form of epitaxy that typically deposit alternating monolayers of two elements onto a substrate. Metal organic CVD (MOCVD), which is a CVD processes based on metal organic precursors, is operated under ultra high vacuum. This technique is widely used in industry for device fabrication due to the growth of high quality thin films.

1.2.3 Other techniques

Electro-deposition is an electro-coating technique by applying an anode and cathode in the electroplating cell. There is no vacuum required and relatively low cost. Large deposition surface and high deposition rate are major advantages. However, it is only applicable for metal or metal alloys and the films quality is not as good as magnetron sputtering. (Hard to grow epitaxial films)

Sol-gel process is a versatile solution process for making ceramic and glass materials. In general, the sol-gel process involves the transition of a system from a

liquid “sol” into a solid “gel” phase. Applying the Sol-gel process, it is possible to fabricate ceramic or glass materials in a wide variety of forms, such as ultra-fine or spherical shaped powders, thin film coatings, ceramic fibers, micro-porous inorganic membranes, monolithic ceramics and glasses, or extremely porous aero-gel materials. It is a simple technique with low cost. However, it has some disadvantages at film quality, surface roughness and thickness limitation.

Thermal spray technique is a coating process in which melted materials are sprayed onto a surface. The coating precursor is heated by electrical or chemical equipment. It has high deposition rate and lower cost. But there is a large amount of impurity of the film and only poly crystal can be manufactured.

LPE technique is quite different compared with other growth technique, such as PVD. The composition of materials for growing is formed as liquid at their melting temperature. Epitaxy layers can be thermodynamically grown on a substrate with the same orientation when the substrates meet oversaturated solution. The film thickness is about 100um and even thicker.

1.3 Applications of metallic multilayer thin films

Metallic multilayer thin films, have received intense interest for the past few decades. Giant magnetoresistance (GMR) is a quantum mechanical magnetoresistance effect observed in ferromagnetic and nonmagnetic alternating metallic layers. Albert Fert in France and Peter Grunberg in Germany, were awarded the 2007 Nobel Prize in Physics for the discovery of GMR phenomenon in 1988. They studied independently

Fe/Cr/Fe trilayers and Fe/Cr multilayers, and observed significant decrease of electrical resistance (1.5% - 50%) in a magnetic field. [1-2] [2] GMR effect leads to the hard disk drive industry and became the only technique used in disk read-and-write heads since 2003. Ferroelectric multilayer films, especially ferroelectric superlattices with the perfect lattice match at the interface, have applications in semiconductor and micro and nano electromechanical system (MEMS and NEMS) devices. [3] In metallic multilayers internal interfaces construction, including the orientation, misfit dislocation, and kinetics, plays a significant role for the performance. Beside strengthening and resistivity, interfaces in metallic multilayers could absorb radiation induced point defects and thus enhance radiation tolerance.[4]

Very often metallic multilayers also possess unusually high strength, which in some cases can be close to the theoretical strength ($30/\mu$, where μ is the shear modulus). The strengthening mechanism in metallic multilayers has been studied both experimentally and theoretically. Interface plays decisive role in strengthening the multilayer composites. A clear layer thickness dependent strengthening phenomenon is often observed and related strengthening mechanisms have been the subject of extensive studies and often lead to debates. Dislocations pile-ups, coherent stress, elastic modulus mismatch, Koehler stress, texture, and intermixing at interface are among some of the important factors that contribute to or dominate the strengthening. A summary of some of these factors on strengthening mechanisms will be briefly discussed in section 1.4.

1.4 Strengthening mechanisms in metallic multilayers

Metallic multilayer materials, typically synthesized by PVD or electro-deposition techniques, exhibit significant increase in strength when the individual layer thickness decreases from micrometer to nanometer length scale [5-7]. In order to understand the impact of different factors on the strength, varieties of multilayer systems have been explored. These include FCC/FCC type, such as Cu/Ni, Cu/Ag, Cu/304 stainless steel, and Cu/330 stainless steel [5-6,8]; FCC/BCC type, such as Cu/Nb, Cu/Cr, Cu/V and Cu/W [5,9]; and BCC/BCC type, such as Fe/Cr [10]. In comparison to the rule-of-mixture estimation by using the strengths of the individual constituent, the strength of multilayers is typically much higher, due to slip discontinuity, lattice constant mismatch, or elastic modulus mismatch, etc.

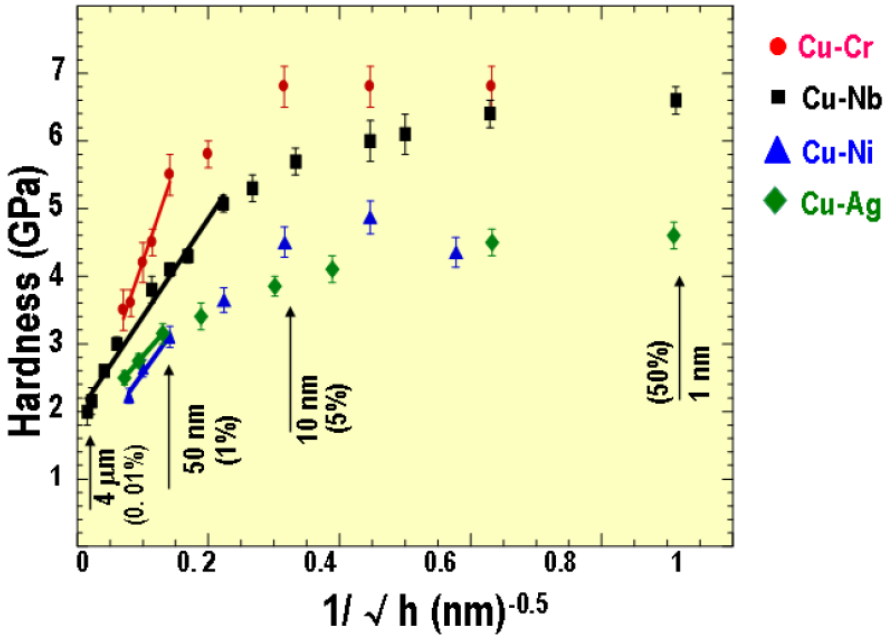

Figure 1.3 Comparison of indentation hardness vs. $h^{-0.5}$ plots for various Cu/X multilayer systems, including Cu/Cr, Cu/Nb, Cu/Ag and evaporated (100) Cu/Ni. Linear

fit at large h is consistent with the Hall-Petch model. At lower h, the Hall-Petch model breaks down[11].

Figure 1.3 shows the indentation hardness of some Cu-based multilayers changing with individual layer thickness (h). When h > 50nm, film hardness increases linearly with $h^{-1/2}$, consistent with the Hall-Petch model. When h decreases to a few tens of nanometers, the Hall-Petch model breaks down. But the film strength continues to increase with decreasing layer thickness. The strengths reach the highest at h of a few nanometers, and then reach a plateau or decreases thereafter, i.e. softening. Softening is observed in highly (100) textured Cu/Ni multilayers. In summary the major deformation mechanisms at different layer thickness can be divided into three regions as illustrated in Figure 1.4[12].

1.4.1 Pile-up based Hall-Petch model

Hall-Petch type of strengthening[13], , where hardness increases linearly with the inverse square root of grain size, is often observed in polycrystalline metals, and thus is often called grain-boundary strengthening, where high strength is induced by crystallites with small grain size. Grain boundaries impede dislocation movement, and the number of dislocations within a grain has an effect on how easily dislocations can traverse grain boundaries to different grains. So by varying the average grain size one can influence dislocation movement and yield strength.

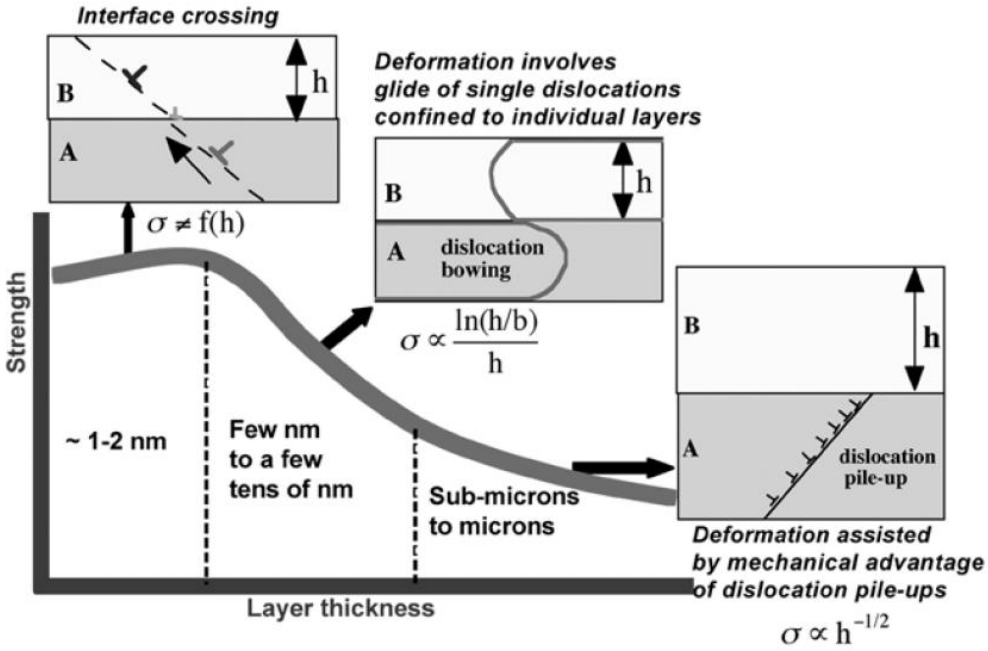

Figure 1.4 A schematic illustration of the deformation mechanisms in metallic multilayers as function of individual layer thickness[12].

As illustrated in Figure 1.4, the hardness scales linearly with $h^{-0.5}$. In this case it is often the layer thickness, h, (often much smaller than average grain size), that is considered as the characteristic features affecting the strength of multilayer composites. Dislocations on the same sliding plane pile up against the interfaces that resist the leading dislocations with a barrier stress (τ^*). When the force on the dislocation reaches the value of resolved shear stress τ_0, dislocations are able to glide. Here τ_0 involves lattice resistance (Peierls stress), solution and precipitation hardening [14]. The number of dislocations that will pile up on the interfaces can be explained as:

$$N = \pi h'(\tau - \tau_0)/G'b \qquad (1.1)$$

where τ is the resolved shear stress across the slip plane, b is Burgers vector of a single dislocation. h' is distance between obstacles on glide plane, and is typically comparable to layer thickness, h. $G' = G/(1-\upsilon)$, where G is the shear modulus, and υ is Poisson's ratio. When the leading dislocation is just able to cross the interface, i.e., when $N(\tau - \tau_0) = \tau^*$, it follows that

$$\tau = \tau_0 + \left(\frac{G'b\tau^*}{\pi h'}\right)^{\frac{1}{2}} \qquad (1.2)$$

which provides the critical resolved shear stress to push the leading dislocation across the interface.

Hall-Petch slope are consistent with the Hall-Petch model, when h is larger than 50nm. Previous work on strengthening of metallic multilayers (such as Cu/Cr, Cu/Nb, Cu/Ni, Cu/330 stain steel, Cu/Ag, Al/Nb, Cu/V) [5,7-8,11] exhibits Hall-Petch regime when h is larger than 50nm. Hardness vs. $h^{-0.5}$ plot is applied to identify the Hall-Petch slope, which is comparable with the calculated slope $k = 0.18G\sqrt{b}$, where b is burgers vector and G is shear modulus of the elastically stiffer phase [5]. From existing studies, such as Cu/Ni multilayers, the single crystalline multilayers shows a lower Hall-Petch slope as compared to polycrystalline multilayers [5]. This also indicated that grain boundaries within layers also contribute to the Hall-Petch slope.

1.4.2 Propagation of single dislocations confined to individual layers

When the layer thickness is less than 50nm, the size dependent hardening is non-linear. Such significant departure in nanoscale regime implies that the deformation is no longer dominated by dislocation pile-ups. Discrete dislocation pile-up is a main

explanation at this range [11,15] Elasticity-based calculations have predicted that, for single ended dislocation pile-ups, $\sigma \propto h^{-0.5}$ is only applicable when the number (N) of dislocation in a pile-up is more than 6 [16]. Decreasing N in proportion to h, especially on smaller length scales, could account for $\sigma \propto h^{-a}$ where $a \neq 0.5$. Typically, when $N < 3$, the dislocation pile-ups are no longer follow H-P relation.

At this range, since the interface barrier to dislocation slip transmission is higher than the gliding resistance, dislocation movement are confined to isolated layers, which can be described by the confined layer slip model (CLS) [17] [18]. As shown in Figure 1.4, the critical resolved shear stress for such confined layer slip model is [19]

$$\tau = \frac{G'b}{2\pi h'} ln\left(\frac{h'}{b}\right) \qquad (1.3)$$

where h' is the distance along the slip plane between adjacent interfaces.

1.4.3 The transmission of a single dislocation across interface

When h is a few nanometers, experimental data indicate that the strength of metallic multilayers reaches a saturation value and no significant strength increase is observed when h further decreases. In this approach, a peak in strength is reached when h is so small until no dislocation pile up can be formed (N <2). The CLS stress, which increases as h decreases, will eventually exceed the interface barrier strength (τ^*), and lead to the event of dislocation crossing interface. The strengthening in this range is affected by coherency stress, misfit dislocations, modulus difference, texture (crystal) orientation, and chemical intermixing along interface.

a. Stress from coherent and incoherent interfaces

Coherent interface is created between two crystals with same crystal structure but different lattice parameters, such as fcc/fcc interfaces. The coherency conditions can be expressed as[20],

$$a_i^A\left(\varepsilon_{ij}^A + 1\right) = a_i^B\left(\varepsilon_{ij}^B + 1\right) \quad (1.4)$$

where a_i^M is the bulk lattice parameter in the ith direction in material M, and ε_{ij}^M is the strain in material M. This equation is accurate in the limit of very small strains. If the coherency strains are very large, coherent interfaces may not form. For example, the lattice mismatch might be so large that the stresses necessary to achieve coherent interface exceed the theoretical tensile strength of one of the components. Additionally, large lattice misfits energetically favor the formation of misfit dislocations, making the interface semicoherent. Then the yield strength of the multilayer films is determined by

$$\sigma = \frac{C^A C^B}{C^A + C^B}\varepsilon \quad (1.5)$$

where C^A and C^B are the effective biaxial elastic constant for each component[21].

Comparing to coherent and semicoherent interfaces, the more complex geometry of interfaces leads to a possible multitude of different atomic configurations. This is called incoherent interfaces and is demonstrated between Cu and Nb. In Cu/Nb multilayers, fcc {111} and bcc {110} planes each contain three low-index atomic directions. An fcc {111} plane contains three <110> nearest neighbor directions while a bcc {110} plane contains two <111> nearest neighbor directions and one <100> direction. Based on this, two commonly observed orientation relations of interfaces between close-packed planes of neighboring fcc and bcc solids can be described. In the

Kurdjumov–Sachs (KS) orientation relation, one of the <110> directions in a fcc {111} plane lies parallel to one of the <111> directions in a bcc {110} plane, and {111} plane is parallel to one of the {110} plane of the bcc crystal. In the Nishiyama–Wassermann (NW) orientation relation, one of the <110> directions in a fcc {111} plane lies parallel to the <100> direction in a bcc {110} plane, and fcc{111} parallel to bcc {110}. Only the introduction of interface dislocations or (martensite) disconnections distinguishes the two cases.

b. Stress from modulus mismatch (Koehler image stress)

The Koehler stress model originates from the large difference in the elastic (shear) modulus between two materials. In a system with a large modulus mismatch, there exists repulsive image stress when a dislocation in "softer" layer crossing the interface to enter a "harder" component. Resolved shear stresses necessary to overcome the repulsive images stress is[22]

$$\tau = bRG \sin\theta / 4\pi h \qquad (1.6)$$

where b is the Burgers vector, $R = \frac{G^A - G^B}{G^A + G^B}$, G^A, and G^B are the shear modulus of materials with higher and lower shear modulus, respectively, h is the distance of dislocation from the interface, and θ is the smallest angle between the interface and the glide plane of crystal. Clearly, the influence of the image stress will become significant when there is a large difference in shear modulus.

Specifically, for Cu/Ni multilayer system, based on eq. 1.6, similar atomistic simulations of the Koehler stress for (a/2)<110> screw dislocations were performed for three different orientation [23]. Table 1 compares the stresses required for the screw

dislocations to overcome the (001), (110) and (111) interfaces of Cu/Ni. The simulation predicts that there is hardness difference for different orientation in a same multilayer system due to Koehler stress.

Table 1 Atomistic simulation results on the Koehler stress for Cu-Ni bilayers along various orientations.

Orientation	[001]	[110]	[111]
Mobility (unites of μ)	0.01	0.011	0.014

c. Texture interaction

For the interactions in an epitaxial interface in the multilayer system, the slip planes are continuous across the interface and the slip vectors identical in the adjoining layers. In this case, considering a FCC/FCC type, (100) and (111) interfaces, (a/2) <110> screw dislocations across the (100) interface directly, but have to cross-slip for transmission of slip across the (111) interface. The blocking strength of cross-slip is substantially larger, and processes such as indirect transmission of slip across the interface as well as the Orowan mechanism become much more probable.

d. Intermixing induced softening

In chemistry, miscibility is the property of two phases to mix in all proportions, forming a homogeneous solution. By contrast, substances are said to be immiscible if in some proportion, they do not form a solution. As depicted in Figure 1.3, at smaller h, only Cu/Ni multilayer system exhibits a softening phenomenon. Compare the phase diagram of Cu with Cr, Ag, Ni and Nb, Cu and Ni is the only miscible multilayer

system. At smaller h, interfaces between Cu and Ni become unclear due to the high possibility to form Cu-Ni solid solutions, and may decrease the effect of coherency stress and Koehler stress on interface resistance. The softening phenomenon is also found in Cu/330 stainless steel (SS) multilayers [6].

1.4.4 Critical thickness to form transparent interfaces

As illustrated in 1.4.2 and 1.4.3, in metallic multilayers, the interfaces become transparent for dislocations to cross and not forming pile-ups at smaller h. The critical thickness of this can be calculated as

$$h_t = \frac{bn}{(1+\upsilon)\epsilon_m} \qquad (1.7)$$

where b is Burger's vector, n =1 when considering edge dislocations pile up [5]. Misfit strain is $\epsilon_m = \frac{2(a^A - a^B)}{a^A + a^B}$, a^A and a^B is lattice parameter for materials in multilayers. Poisson ratio υ is 0.3.

1.5 Twinning

Twinning occurs when two separate crystals share some of the same crystal lattice points in a symmetrical manner. Twins can be obtained as a result of different processing techniques. These are:

a. Deformation (mechanical) twins

b. Annealing twins

c. Growth twins

Deformation and annealing twins are defects generated by mechanical and thermal annealing techniques. In thin films material, rolling, stretch and high deposition rate are some techniques to form deformation twins [24-25]. Growth twins can be obtained by using sputtering or electro-deposition techniques. Initial nuclei that form maybe either "perfect" or have stacking faults and /or twins. The critical size (r*) of perfect and twined nucleus case can be calculated by [6]

$$r^*_{perfect} = \frac{\gamma}{(\frac{kT}{\Omega} ln\left[\frac{J\sqrt{2\pi mkT}}{P_s}\right])} \quad (1.8)$$

$$r^*_{twin} = \frac{\gamma}{(\frac{kT}{\Omega} ln\left[\frac{J\sqrt{2\pi mkT}}{P_s}\right] - \frac{\gamma_t}{h})} \quad (1.9)$$

where k is the Boltzmann constant, T is the substrate temperature during deposition, Ω is the atomic volume, J is the deposition flux, Ps is the vapor pressure above solid, m is the atomic mass of depositing species, $\gamma_t$is the twin boundary energy. We note that the volume free energy difference, $\Delta G_v = \frac{kT}{\Omega} ln\left[\frac{J\sqrt{2\pi mkT}}{P_s}\right] > 0$. Comparing Eq.1.8 and Eq. 1.9, typically, if $\gamma_t$is very low and ΔG_v is very high, the difference between $r^*_{perfect}$ and r^*_{twin}will be negligibly small, and the formation of twinned nuclei may occur with higher probability during growth. Therefore, low γ_t and high deposition rate will enhance the formation of nanoscale twins.

Nanotwins with spacing of a few tens of nanometers, which contribute significant enhancement of the strength, have been observed in several metallic materials, including sputtered Cu [24,26-28], 330 stainless steel (SS) [6], Pd[29], and electro-deposited Cu [25]. Low stacking fault energy (SFE) and twin boundary (TB) energy, which provide low energy barrier to form growth twins, are critical to form nanotwins

in Cu and 330 SS. However, for materials with high SFE, it is possible to form misfit twins on a substrate with different elastic constant and lattice parameters, such as Pd/Ni[29]. The energy to form twins E_f can be expressed as[30]

$$E_f = E_{s,twin} + E_{int,twin/misfit} + \Gamma_t \quad (1.10)$$

$$E_{int,twin/misfit} = \frac{2\mu(1+\upsilon)}{(1-\upsilon)} f m b_1 h \quad (1.11)$$

$$\Gamma_t = \frac{2\gamma_t h}{sin\phi} \quad (1.12)$$

where Γ_t and γ_t is the total and specific twin boundary energy between the misfit twin and the matrix, $E_{s,twin}$ and $E_{int,twin/misfit}$ is the self energy of the twins and the interaction energy between the twin and the mismatch strain, respectively. μ and υ are shear modulus and Poisson's ratio of the material. Mismatch strain, f can be expressed as $f = 2 \times \frac{a_f - a_s}{a_f + a_s}$, where a_f and a_s denote the lattice parameters of the film and substrate. h is the twin thickness and b_1 is Burgers vector. The product of the b_1 and f must be negative to ensure negative interaction energy, which is necessary to reduce E_f, then increase the possibility to form misfit twins ($E_f < E_{s,twin}$). ϕ is the angle between the twin boundary and substrate surface. The detail of $E_{s,twin}$ is calculated by using shear modulus and burgers vector in both substrate and film [30]. We note that the critical thickness of misfit twinning is the smallest twin width to reach the smallest E_f.

1.6 Motivation and objectives

1.6.1 Strengthening mechanisms in highly textured Cu-Ni multilayers

As illustrated in 1.4, the strengthening mechanism in Cu/Ni multilayers has been extensively studied [5,11,15,23,31]. However, there are two major objectives to study on highly textured Cu-Ni multilayers.

a. Comparison between (111) and (100) textured Cu/Ni

Except atomistic modeling, no experimental results showed the hardness differences between (111) and (100) Cu/Ni multilayers at different h. This may confirm the Koehler stress and texture interaction assumption of strengthening in different textured multilayer films. Also there is a large discrepancy in hardness data of Cu/Ni multilayers fabricated by using different technique or by different groups. The plot of hardness vs. $h^{-1/2}$ can be quite different in many cases. A reliable set of hardness data for Cu/Ni multilayer with different texture is clearly needed to facilitate the understanding of strengthening mechanism via atomistic and analytic modeling.

b. Twin interface induced strengthening in multilayers

Twin boundaries may affect the strengthening in (111) Cu/Ni multilayers. Such an effect is simulated by MD simulations, but its significance is not proved experimentally in multilayers. Hence the impact of twin interface on strengthening is often neglected. In large contrast to the misconception, we prove direct evidence of significant strengthening in twinned Cu/Ni multilayers.

1.6.2 Growth twins in Ni

Ni has relatively high stacking fault energy, and hence the formation of twins in Ni is in general very difficult. In this study, we show that high density twins can form in Ni, facilitated by the coherent nature of {111} textured Cu/Ni interface in fine multilayers.

CHAPTER II

EXPERIMENTAL METHODS

2.1 Fabrication of highly textured Cu-Ni multilayers

Magnetron sputtering is a technique used to produce highly textured Cu-Ni multilayer films in this work. Good adhesion and stoichiometric control are the main reasons to choose the magnetron sputtering technique. The basics of sputter deposition are illustrated in the introduction section. Here only a brief description of magnetron sputtering technique is discussed. Compare to the other sputtering techniques, magnetron sputtering is more effective in achieving higher deposition rate. Because magnetic fields trap the electrons uniformly close to the surface of a target as shown in Figure 2.1 A magnetron has one or two magnitudes more current than DC discharges at the same power [32].

A parallel magnetic field is superposed on the glow discharge. Electrons in the glow discharge show circular motion. The orbit drifts in the direction of the E × M, where E and M denote the electric field in the discharge and the magnetic field. Magnetic field is oriented as these drift paths for electrons form a close loop. This causes an increasing rate of collision between the electrons and the sputtering gas molecules such as Argon. The magnetic field causes an increase of the plasma density that leads to increased current density at the cathode, and then raises the sputtering rate of the system [33].

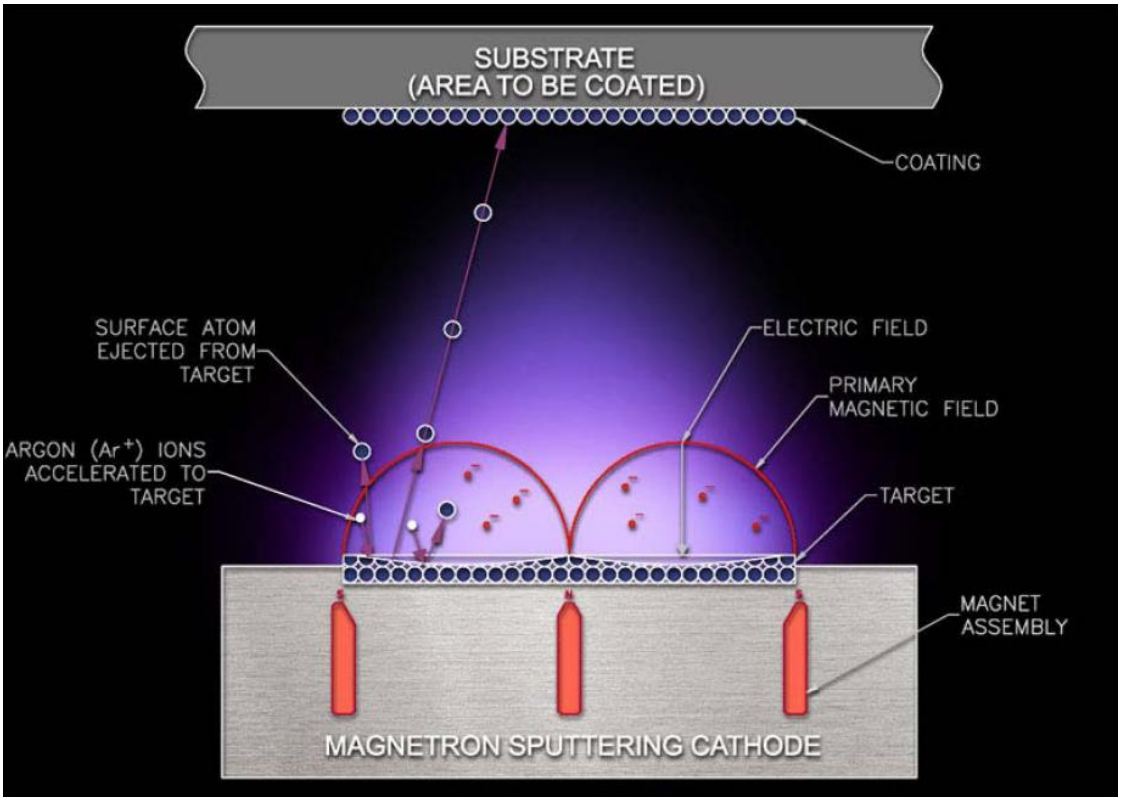

Figure 2.1 Working principle of magnetron sputtering. [32]

Sputtering with a transverse magnetic field produces several important modifications. Target-generated secondary electrons do not bombard substrates because they are trapped in circular trajectories near the target. Therefore, these electrons do not contribute to increased substrate temperature and radiation damage. This allows the use of temperature-sensitive (ex. Low melting temperate), and surface sensitive (ex. Micro electro-mechanical devices) substrates with low inverse effects. In addition, this class of sputtering sources produces higher deposition rates than conventional sources and lends itself to economic, and large-area industrial application. It is important to check

the resistance between the anode shield and target clamp after changing the targets in order to avoid shorting out problems.

Cu (99.995%) and Ni (99.99%) targets were used for DC magnetron sputtering to deposit Cu/Ni multilayers. For epitaxial growth, single crystal substrates of Si (100), (110) were etched in HF to remove the SiO_2 layer. After etching the substrates were loaded into chamber immediately. The chamber was evacuated to less than 5×10^{-8} torr prior to deposition. Cu and Ni target are also pre-sputtered to remove the contamination on the target surface. All the depositions are performed at room temperature. No heating or cooling was applied to the substrate during deposition. Inside the vacuum chamber, a thermocouple is placed on the Aluminum sample holder to monitor the temperature fluctuations. The temperature was usually around 50~60 ^{0}C at most during deposition. The deposition rates were constant at 0.59nm/s for Cu, 0.55nm/s for Ni by controlling the DC power to the magnetron gun and the distance between targets to substrate. A 100 ~ 200 nm Cu seed layer was deposited before the deposition of multilayers. The individual layer thickness is identical and varies from 1 to 200 nm for different samples. The total thickness of films was ~ 1.5um for multilayers with h of 100 nm or less, and ~ 4 um when h is larger than or equal to 100nm.

2.2 Microstructure characterization

2.2.1 X-ray diffraction (XRD)

X-ray diffraction is a non-destructive tool for the structural analysis of multilayer films. During the XRD experiments, the samples are exposed by X-ray

monochromatic beam from a Cu-Kα source. XRD is used to investigate the crystal structure with a wavelength of 1.5405 Å. The multilayer film samples scatter the incident x-ray beam in all directions. The scattered x-ray also mutually reinforce in certain directions due to the periodic arrangement of atoms on specific crystallographic plans in the crystalline solid films. The position of the diffracted beam is given by the Bragg's law:

$$n\lambda = 2d \sin \theta \qquad (2.1)$$

where n is an integer determined by the order given, λ is the wavelength for the incident x-ray beam, d is the spacing between the planes in the atomic lattice, and θ is the angle between the incident x-ray beam and the scattering crystallographic planes. Figure 2.2 shows diffraction according to Bragg's law. [34]

During the XRD experiments on the metallic multilayer systems, when individual thickness (h) is equal or less than 5nm, superlattice effect will affect the peak position. It is due to the influence of interfacial constraint on lattice parameter of multilayers. The constraint is more significant at smaller h [35-36]. When the evolution of peak positions has the greater magnitude, and the structural coherency length, is larger than bilayer thickness (ʌ), the peak position can be calculated by: [35]

$$\frac{2sin\theta}{\lambda} = \frac{1}{\bar{d}} \pm \frac{n}{\Lambda} \qquad (2.2)$$

where λ is the wavelength of x-ray, n is satellite order, $\bar{d}$ is the average lattice constant. $\bar{d}$ = ʌ/ (N_A+N_B) where N_A and N_B are the number of atomic planes of material A and B in one bilayer. $\bar{d}$ & ʌ are the only quantities that can be determined directly from the peak positions.

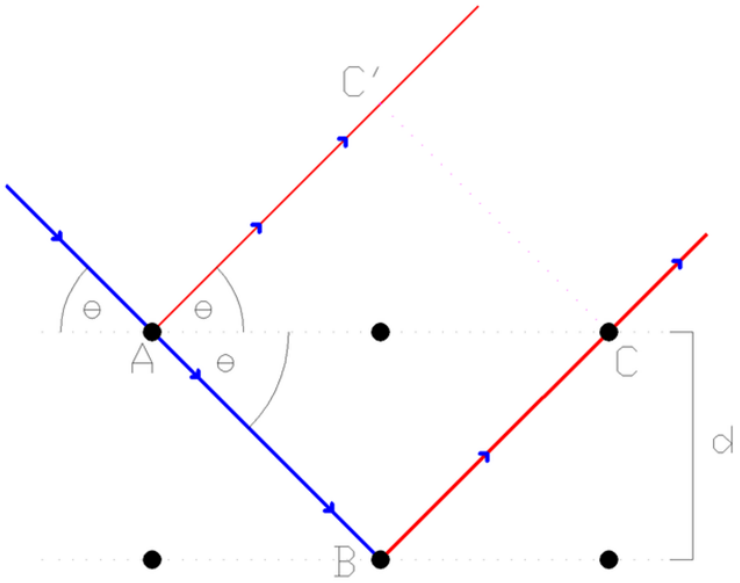

Figure 2.2 Schematic representation of the diffraction according to Bragg's law.

The XRD experiments were performed at room temperature by Bruker Powder Diffractometers (D8 - Discover) in the X-ray Diffraction Laboratory in the Department of Chemistry. Bruke D8 – Discover X-ray powder diffractometer is equipped with Cu-Kα source anode, D8 Goniometer, graphite monochromator on the diffracted beam and Lynxeye PSD for detection. The angle between the direct x-ray beam and the diffracted beam is 2θ, where θ is the Bragg angle between beam and crystal planes. The divergent x-ray beam of filtered or monochromatized radiation impinges on the flat face of a sample. The sample is rotated at precisely half of the angular speed of receiving slit in order to maintain a constant angle between the incident and diffracted beam.

2.2.2 Transmission electron microscopy (TEM)

Transmission electron microscopy (TEM) is a critical technique in microstructure characterizations of sputtered multilayer films. In TEM equipment, a high energy electron beam is transmitted through an ultra thin specimen (~100 nm). Electrons interact with specimen and pass through, and then form an image. The imaging devices can be fluorescent screen, photographic film, or charge-coupled device (CCD) camera.[37]

TEM and High-Resolution TEM (HRTEM) were performed on JEOL 2010 microscope in the microscopy and imaging center (MIC). JEOL 2010 is equipped with a Gatan SC1000 ORIUS CCD camera (Model 832), by using 200KV accelerating voltage with a LaB_6 filament. The microscope has 0.23 nm point-to-point resolution.

2.2.3 Scanning transmission electron microscopy (STEM)

Scanning transmission electron microscopy (STEM) is a type of TEM techniques that can characterize the chemistry of materials. The rastered electron beam focuses into a narrow spot across the sample. This microscope is suitable for analysis techniques such as energy dispersive X-ray (EDX) spectroscopy, electron energy loss spectroscopy (EELS) and annular dark-field imaging (ADF). These signals can be obtained simultaneously. By using STEM, it is possible to form atomic resolution images where the contrast is directly related to the atomic number. Intermixing between layers in multilayer films can be identified by using the STEM line profile technique.

However, considering the limitation of the narrow spot size, the EDX spectroscopy of layer profiles could not be separated perfectly.

STEM and EDX were performed on FEI Tecnai G2 F20 microscope in the Microscopy and Imaging Center (MIC). FEI Tecnai G2 F20 microscope is equipped with Fischione ultra-high resolution STEM HAADF detector (0.23nm in the STEM image mode) and Oxford instruments EDX detector with a spatial resolution of ~1-2nm. The calibrated spot size is 1.5nm.

2.3 Nanoindentation

2.3.1 Definition of hardness

The material mechanical properties reflect the responses or deformations to an applied load or force. Hardness indicates the resistance of a material to localized plastic deformation or to permanent penetration by another hard material. A higher hardness will lead to higher resistance to plastic deformation and better wear resistant properties. The advantages of using nanoindentation are avoiding the dimension constraint effect of the grain size and dislocation spacing. Measuring hardness using nanoindentation involves two steps. At first, a small and hard indenter is pressed into the material with a load F and the displacement is composed of elastic and plastic deformation. Secondly, the elastic deformation is recovered and only the residual area which is due to plastic deformation can be measured when the indenter is retracted [38]. The hardness is defined by

$$H = P/A \qquad (2.3)$$

where H is the hardness, P is the load and A is the residual area. Figure 2.3 shows the schematic diagram of the cross-section of an indentation. The harder the material, the smaller and shallower is the indent.

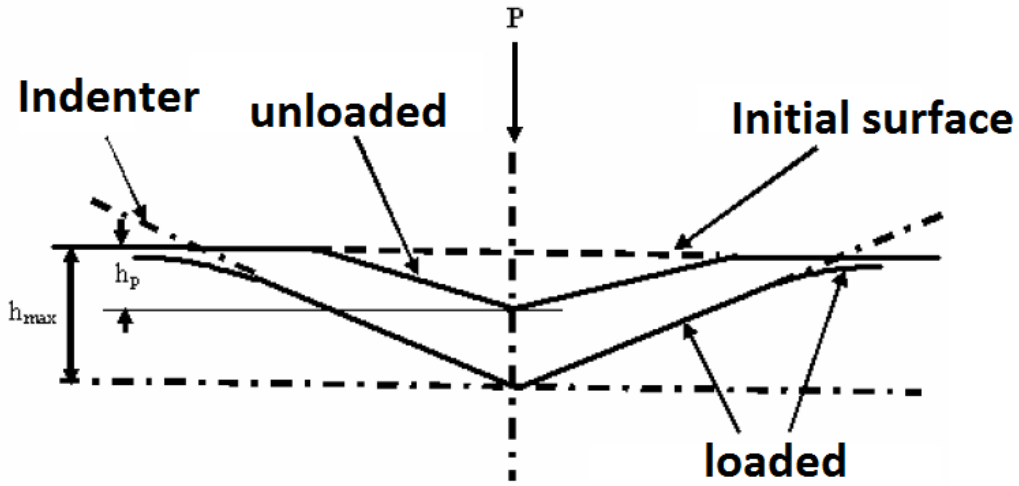

Figure 2.3 A schematic diagram of the cross sectional of an indentation.

2.3.2 Determination of indentation hardness

The indentation hardness (H_{IT}) represents the hardness of materials measured by nanoindentation. HIT is determined by equation (2.4) where P_{max} is the maximum applied force and A_c is the projected area of the contact between the indenter and the material surface.

$$H_{IT}=P_{max}/A_c \qquad (2.4)$$

A_c could not be measured directly. An area function, which describes the shape of the indenter tip, has to be expressed as a mathematic function relating to the depth of contact of the indenter with h_c. The indentation hardness measurement process is similar to the conventional techniques since hardness values are directly obtained from the

load-displacement curve. However, they are sensitive to the data analysis methods including elastic contact model [39], continuous stiffness method [40], and contact solution for spherical indenters[41]. Among these, the analysis based on elastic contact model [39] is the most commonly used method. It can be applied to determine the indentation hardness of thin films as well. It assumed: (1) deformation upon unloading is purely elastic; (2) the compliances of the samples and of the indenter tip can be combined as springs in series and (3) the contact can be modeled using an analytical model for contact between a rigid indenter of defined shape with a homogeneous isotropic elastic half space using the equation as below.

$$S = \frac{2E_r\sqrt{A_c}}{\sqrt{\pi}} \tag{2.5}$$

where S is the contact stiffness, A_c is the contact area, and E_r is the reduced modulus.[39]

Based on these assumptions, contact depth h_c can be expressed by

$$h_c = h_{max} - \varepsilon(h_{max} - h_i) \tag{2.6}$$

where h_{max} is the maximum depth of indentation, and h_i is the intercept depth of the maximum unloading indentation. The correction factor ε is a function of the shape of the indenter tip, for example, 1 for flat, 0.73 for conical, 0.75 for Berkovich, Vickers and spherical indenter.

The procedure for data analysis to obtain indentation hardness is as follows: The slope of the tangent at P_{max} is used to obtain h_i, and h_{max} at P_{max} is acquired in load-displacement curve shown in Figure 2.4. Correction factor ε is determined by the shape of indenter tip. So the contact depth h_c can be obtained by inputting h_i, h_{max} and ε according to Eq. 2.6. The project area A_c is a function of shape of indenter tip. For a

Vickers indenter, a pyramid shape with a square base, $A_c = 24.5 \times h_c^2$. For a perfect Berkovich indenter, a diamond pyramid with triangular base, $A_c = 23.96 \times h_c^2$. Then, the indentation hardness can be obtained according to Eq. 2.4.

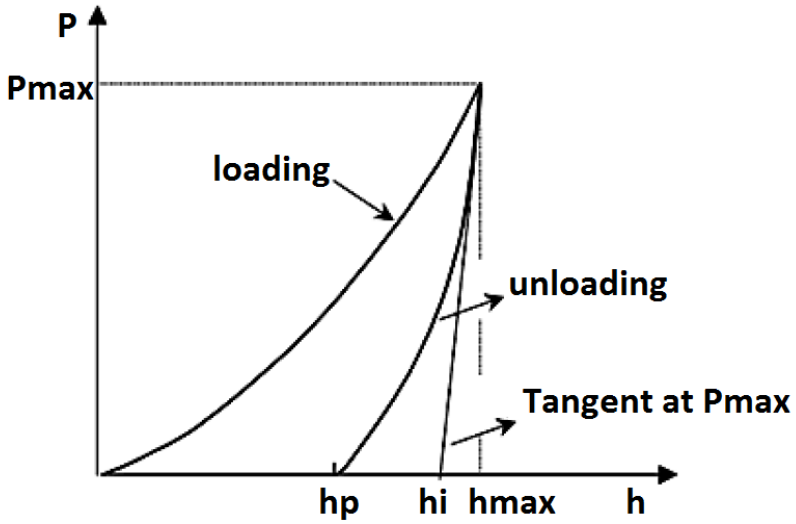

Figure 2.4 A schematic diagram of a loading-unloading curve during indentation.

2.3.3 Determination of indentation modulus

The elastic contact model assumes that the compliance of the samples and of the indenter tip can be combined as springs in series. Therefore,

$$\frac{1}{E_r} = \left(\frac{1-\nu_{indenter}^2}{E_{indenter}}\right) + \left(\frac{1-\nu_{IT}^2}{E_{IT}}\right) \qquad (2.7)$$

where E_r is called reduced modulus, $E_{indenter}$ is the modulus of indenter and E_{IT} is modulus of the tested specimen, $V_{indenter}$ and V_{IT} is the Poisson's ratio of the indenter and the tested specimen, respectively. From Eq. 2.5, the reduced modulus is obtained by contact stiffness and projected area as below.

$$E_r = \frac{S\sqrt{\pi}}{2\sqrt{A_c}} \quad (2.8)$$

According to Eq. 2.7 and Eq. 2.8, the indentation modulus (E_{IT}) can be obtained by combining these two equations:

$$E_{IT} = \frac{1-\nu_{IT}^2}{\frac{2\sqrt{A_c}}{S\sqrt{\pi}} - \left(\frac{1-\nu_{indenter}^2}{E_{indenter}}\right)} \quad (2.9)$$

The indentation modulus is comparable to the Young's modulus of the material. Results from this technique may be influenced by many factors such as tip geometry, machine compliance, time-dependent displacements, surface roughness, indentation size, etc.

2.3.4 Measurement of thin film hardness

Cu/Ni multilayer films hardness was measured by a Fischerscope HM 2000XYp nano/microindentor with a Vicker's indenter. The indentation depth and a constant, specific to each indenter tip, are used to calculate the area of the indenter displacement. The positioning devices consist of the holding device for the measuring head and a microscope with an attached video camera for examining the test area. Manually adjustable XY measuring stage and programmable XY measuring stage are equipped. The coordinates of the measurement points can be programmed and tested automatically in sequence. The load range is constant at 0.4 to 2000 mN and the maximum indentation depth of the indenter is 150 μm. The hardness and indentation modulus of metallic multilayer films were measured based on an average of 9-12 indents at different indentation depths at room temperature with the same loading rate.

In this Cu/Ni multilayers hardness measurement, the load is constant at 300 mN. 16 indents were made at each indentation depth. Loading time is 30 seconds. The multilayers indentation hardness was determined by eliminating substrate and soft seed layer effect when the indentation depth is around 10% of total layer thickness.[42]

CHAPTER III

RESULTS AND DISCUSSION

During deposition, a Cu seed layer is applied between the substrate and multilayers to assist the fabrication of highly (100), (111) textured Cu/Ni multilayers. A schematic shown in Figure 3.1, represents the deposition processes and orientation relation between textured {111} films on Si (110) substrates. Details of epitaxial orientation between film and substrate will be discussed in detail later.

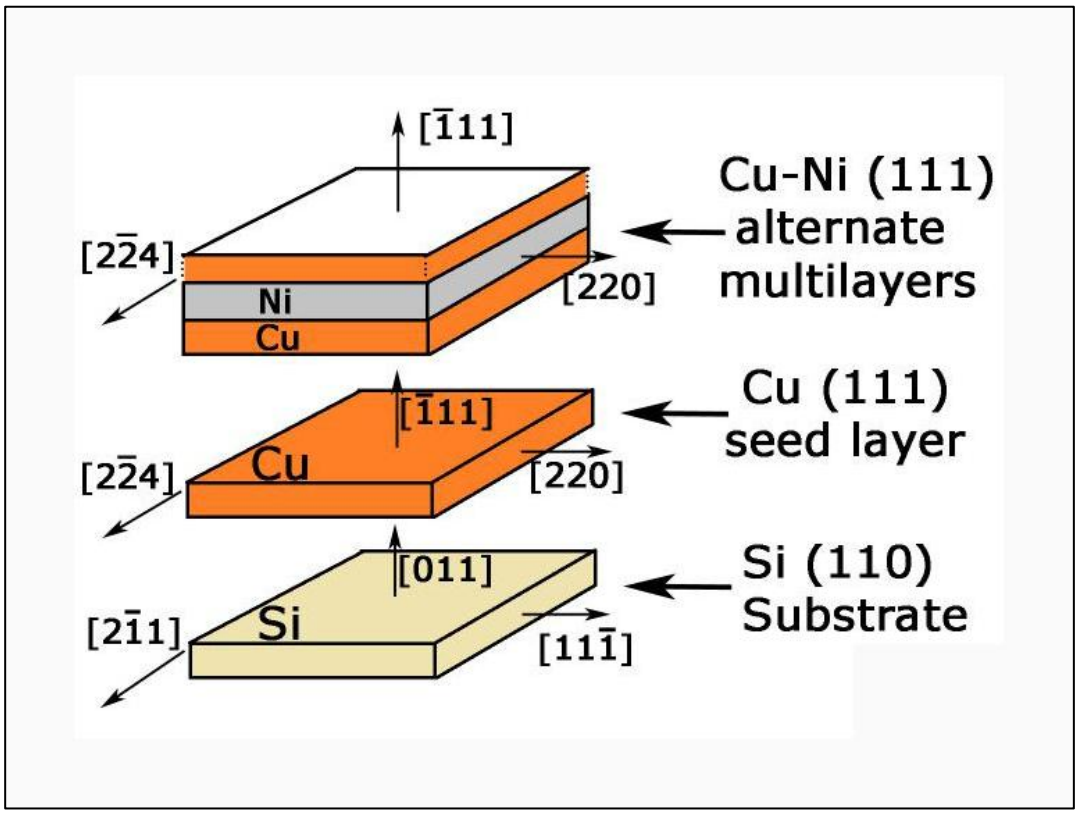

Figure 3.1 A schematic of highly (111) textured Cu/Ni multilayer on Si (110) substrate coated with Cu seed layer.

3.1 Microstructure

3.1.1 X-ray diffraction results

XRD patterns of as-deposited Cu/Ni multilayers on Si (100) and (111) substrates in Figure.3.2 reveal strong Cu and Ni (100) and (111) texture on Si (100), Si (110) substrates, respectively. When h is greater than 10 nm, the Cu and Ni diffraction peaks (such as (100) diffractions) are clearly distinguishable. Satellite peaks are prominent when h is 10 nm or less, in (111) textured multilayer, whereas they are clearly identified when h is 5 nm or less in (100) textured multilayer. A diffraction peak with lattice spacing of 2.056 Å and 1.780Å becomes the dominant peak (in terms of peak intensity) when h is 2.5 nm or less in {111} and {100} textured systems. This peak position corresponds to the average lattice spacing of Cu and Ni (100) or (111) planes. Figure 3.3 analyzes super-lattice peaks by applying $\frac{2\sin\theta}{\lambda} = \frac{1}{\bar{d}} \pm \frac{n}{\Lambda}$ (equation (2.2)) in (111) textured multilayer at h = 10 or 2.5 nm. When h is 10 nm, Cu and Ni (111) diffraction peaks corresponding to bulk lattice parameters are still visible, and are decorated with the first order superlattice (satellite) peaks. The peak labeled with "1" represents the overlapped superlattice peaks of Cu and Ni (111), d_0. When h decreases to 2.5 nm, the peak with the average lattice parameter of d_0 appears dominant, with the first order superlattice peaks arranged symmetrically on each side.

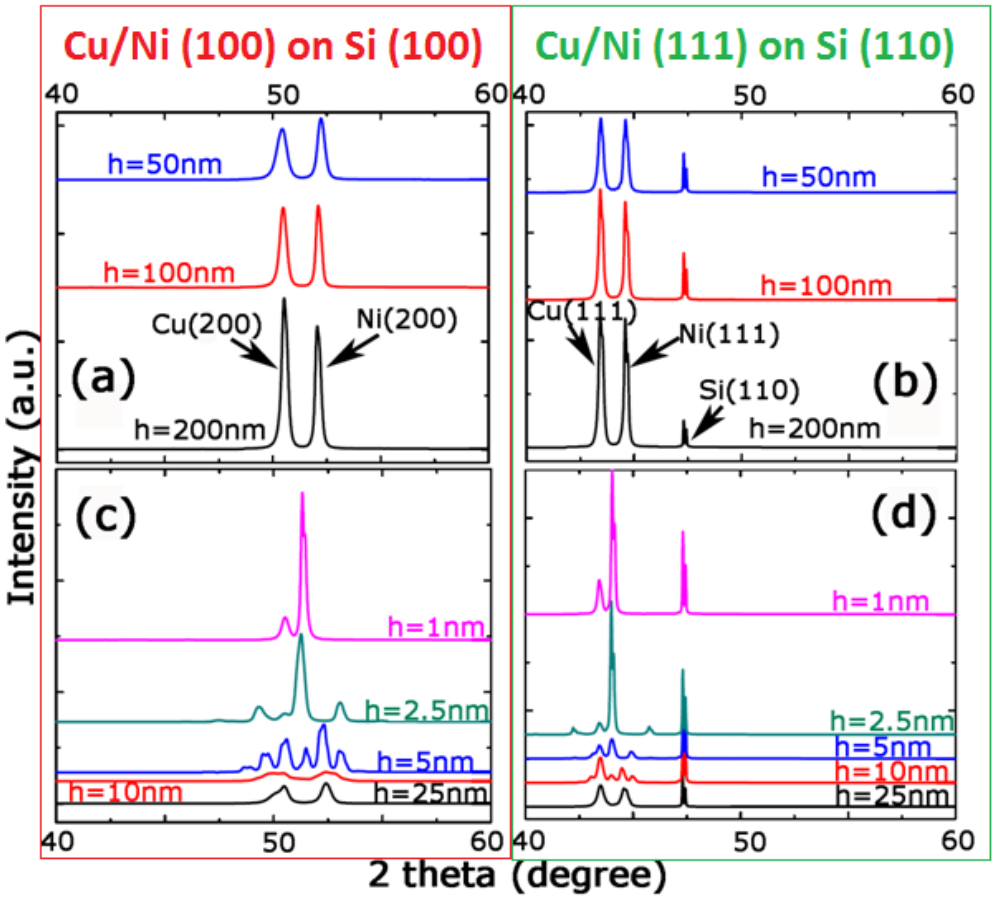

Figure 3.2 X-ray diffraction (XRD) patterns show Cu/Ni multilayers textures: (a), (c) (200) on Si (100); (b), (d) (111) on Si (110). Satellite peaks are noted for each layer thickness equal to or less than 10nm.

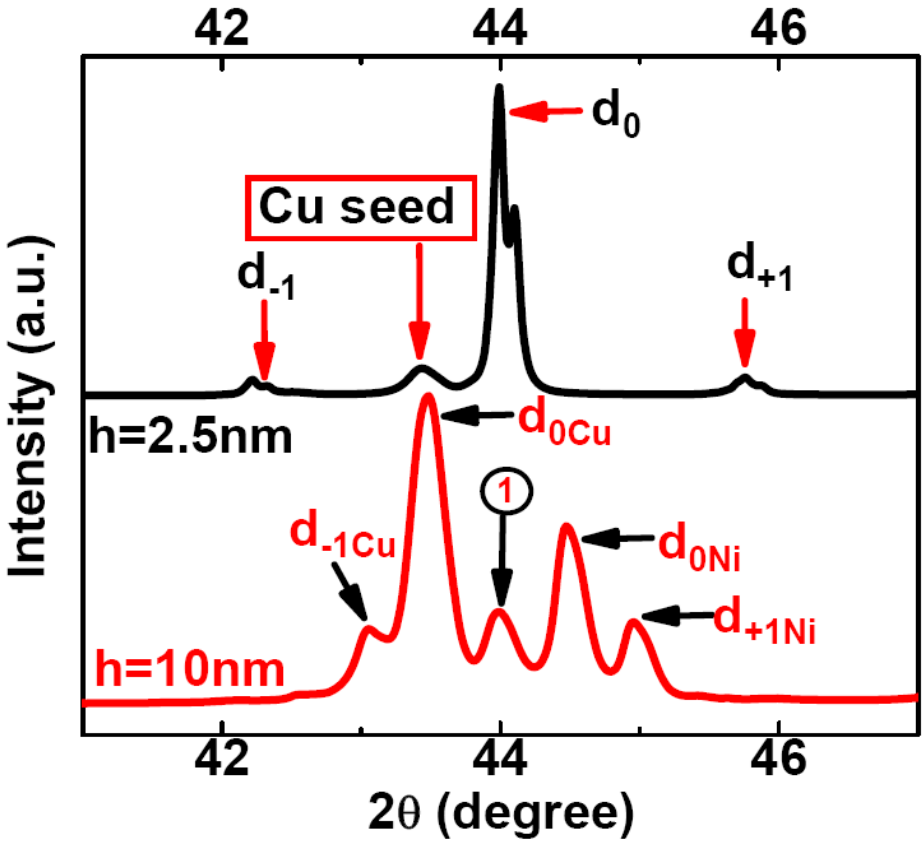

Figure 3.3 Super-lattice peaks in (111) texture multilayer at h = 10nm or 2.5nm. When h is 10nm, the super-lattice peaks are related to lattice-spacing of bulk (111) Cu and Ni. The super-lattice peaks is related to average lattice spacing of Cu and Ni (111) planes at h = 2.5nm. "(1)" is the overlap of both super-lattice peaks of Cu and Ni.

3.1.2 Electron microscopy results

Bright field cross-sectional TEM image of as-deposited Cu 2.5 nm / Ni 2.5 nm (referred to as Cu/Ni 2.5 nm thereafter) multilayers on Si (100) show strong (100) texture in Figure 3.4. The inserted selected area diffraction (SAD) pattern clearly demonstrates the epitaxial Cu/Ni (100) orientations in the films. The compositional line scan obtained from STEM studies demonstrates chemically alternating layer structures in Cu/Ni 2.5 nm multilayers.

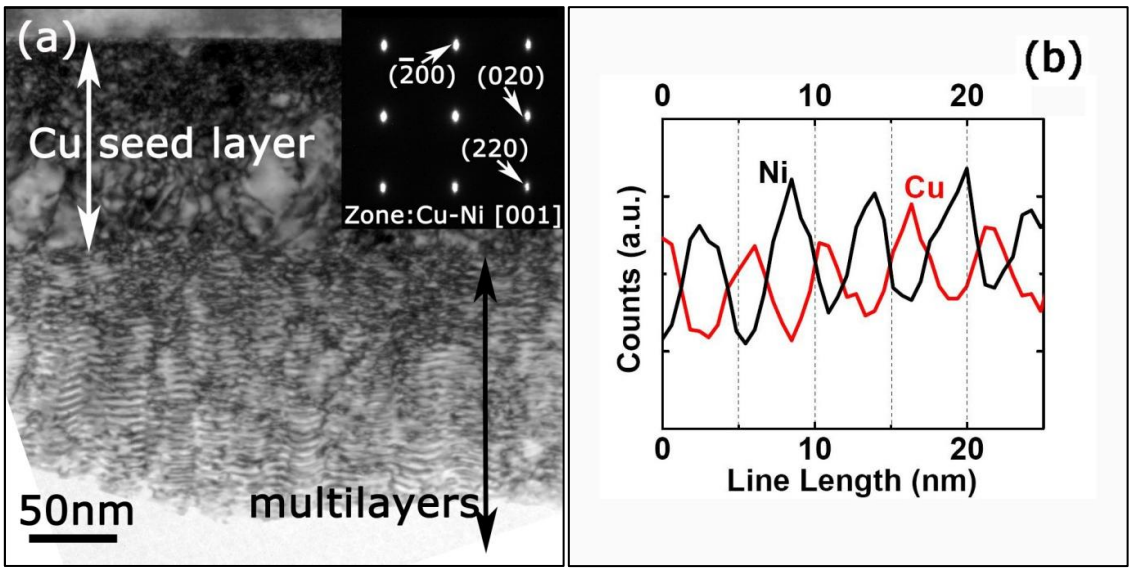

Figure 3.4 A bright field cross-sectional TEM image and STEM line profiles of as deposited Cu 2.5nm/ Ni 2.5nm multilayers on Si (100). (a) The inserted selected area diffraction (SAD) pattern indicates a strong (200) texture. (b) Morphology and line profile show the clearly distinguishable layer interfaces.

Figure 3.5 and Figure 3.6 are the bright field cross-sectional TEM images of Cu /Ni 100 nm and Cu /Ni 10 nm multilayers on Si (110) substrates examined along Si <110> zone axis. In Figure 3.5, the SAD pattern clearly confirms the strong (111) texture in Cu/Ni 100 nm multilayer. At large layer thickness, twins are occasionally and

primarily observed in Cu in (111) textured multilayers. A red square magnifies several twins in a columnar grain in Cu layer. In Figure 3.6, the micrographs and inserted STEM compositional line profile show chemically modulated layer structure in Cu/Ni 10 nm multilayer, and the inserted SAD pattern indicates a strong (111) texture.

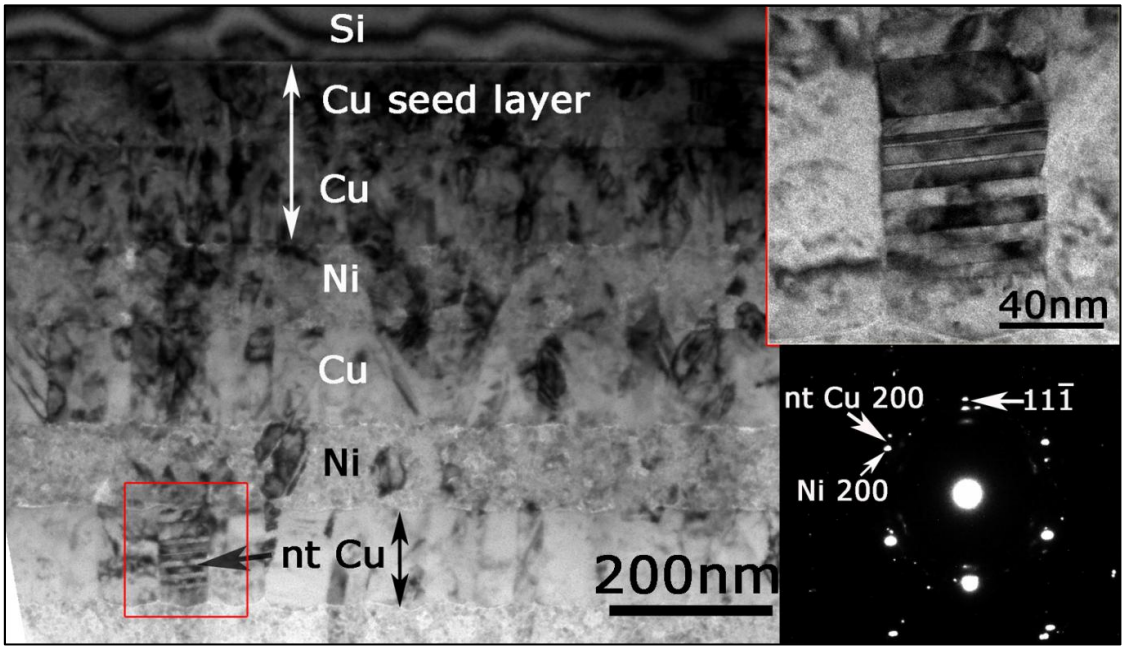

Figure 3.5 A bright field cross-sectional TEM image of as deposited Cu 100nm/ Ni 100nm multilayers on Si (110). The inserted SAD pattern indicates a strong (111) texture of multilayers. Image shows the clear layer interface and nanotwins in Cu layer. In highly (111) textured multilayers, nanotwins are observed only in Cu layer at large layer thickness.

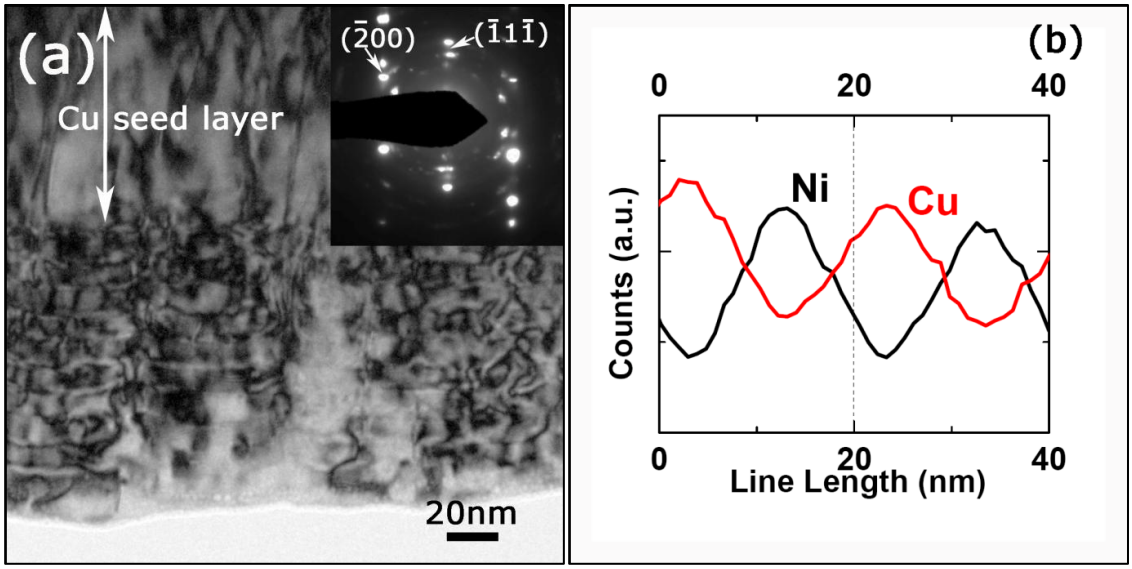

Figure 3.6 A bright field cross-sectional TEM image and STEM line profiles of as deposited Cu 10nm/ Ni 10nm multilayers on Si (110). (a) The inserted selected area diffraction (SAD) pattern indicates a strong (111) texture. (b) Morphology and line profile show the clearly distinguishable layer interfaces.

The Cross-sectional bright field TEM micrograph of highly (111) textured Cu /Ni 2.5nm examined along Si <110> zone axis on Si (110) substrate, as shown in Figure 3.7, reveals that high density twins are oriented normal to the growth direction and clearly extend across both Cu and Ni layers. STEM image and compositional line profile in Figure 3.7(b) show chemically modulated layer structure with insignificant intermixing. Statistical studies, Figure 3.7 (c) and (d) show that the average twin spacing is ~ 3 nm, the same as the individual layer thickness, and the average domain size is about 60 nm.

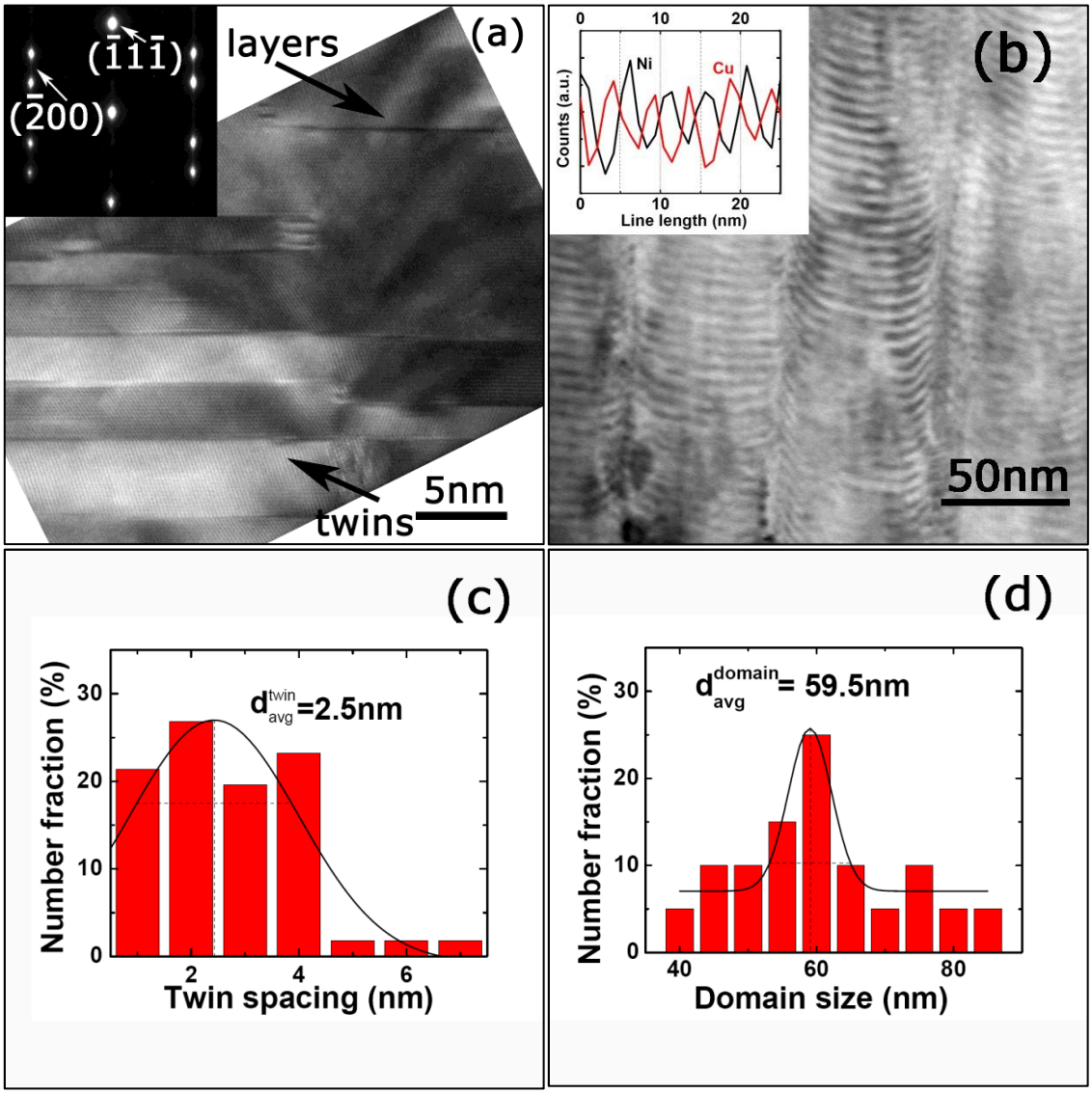

Figure 3.7 Bright field cross-sectional TEM images of Cu 2.5nm/Ni 2.5nm on Si (110) at (a) [220], and (b) [$2\bar{2}4$] multilayers direction. (a) The inserted SAD pattern indicates a strong (111) texture and spots elongation. Nanotwins are observed at [220] direction in both Cu and Ni. Parallel twin boundaries penetrate into curved layer interfaces. (b) Clear layer interface and less intermixing are observed at [$2\bar{2}4$] direction. Statistical distribution of (c) twin spacing and (d) domain size are collected.

To investigate the correlation between layer interface and twin interface, HRTEM studies were performed at two locations. As shown schematically in Figure 3.8 (a), in one case, the twin interface is approximately parallel to layer interface as indicated by box b. The Fast Fourier Transform (FFT) of HRTEM micrograph with filtered planes of Cu/Ni 2.5 nm multilayer taken at this location indeed reveals misfit dislocations along layer interface. It is clear that twin interfaces exist in both Cu and Ni layers. In another case as shown in Figure 3.8 (b), the twin interface and layer interface are inclined relative to each other. The layer interfaces are decorated with misfit dislocations as confirmed by the filtered HRTEM image in Figure 3.8 (c).

Figure 3.9 shows the cross-sectional TEM images of epitaxial Cu / Ni 1 nm films with (111) texture on Si (110) substrate examined along Si <110> zone axis. High density nanotwins that run across layer interfaces are also observed. The inserted SAD pattern indicates a strong (111) texture with typical {111}s coherent twin interface. HRTEM micrograph shows groups of parallel twin interfaces running both parallel and across layer interfaces. Statistical distribution of domain size and twin spacing plot in Figure 3.9 (b) and (c) show that the twin spacing is ~ 16 nm, much smaller than the average domain size, ~ 68 nm.

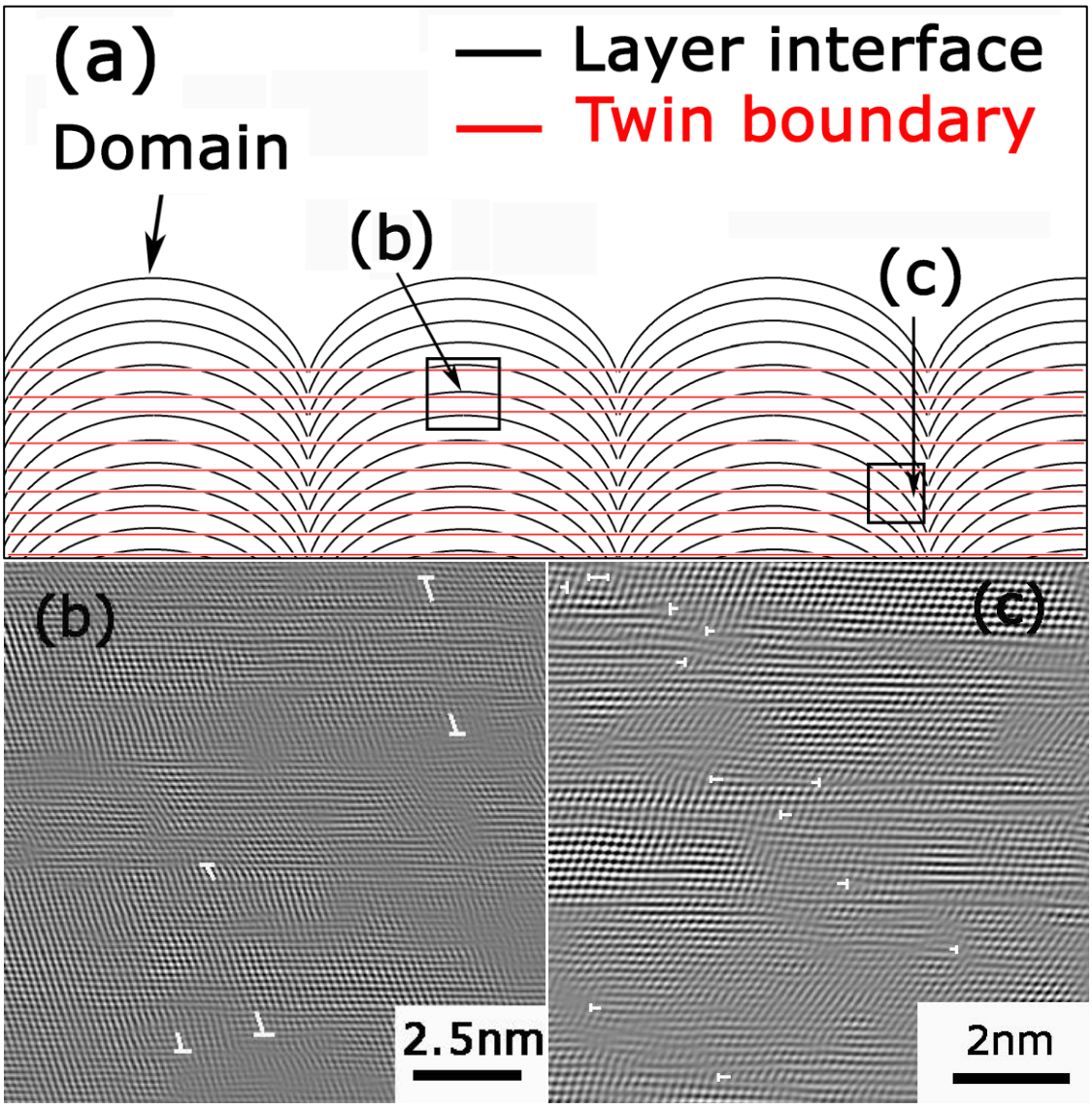

Figure 3.8 (a) A enlarged schematic of twins that penetrate into layer interfaces in highly (111) textured Cu 2.5nm/Ni 2.5nm multilayers. Fast Fourier Transform (FFT) of high resolution TEM (HRTEM) images at (b), (c), confirm the twin boundary penetration.

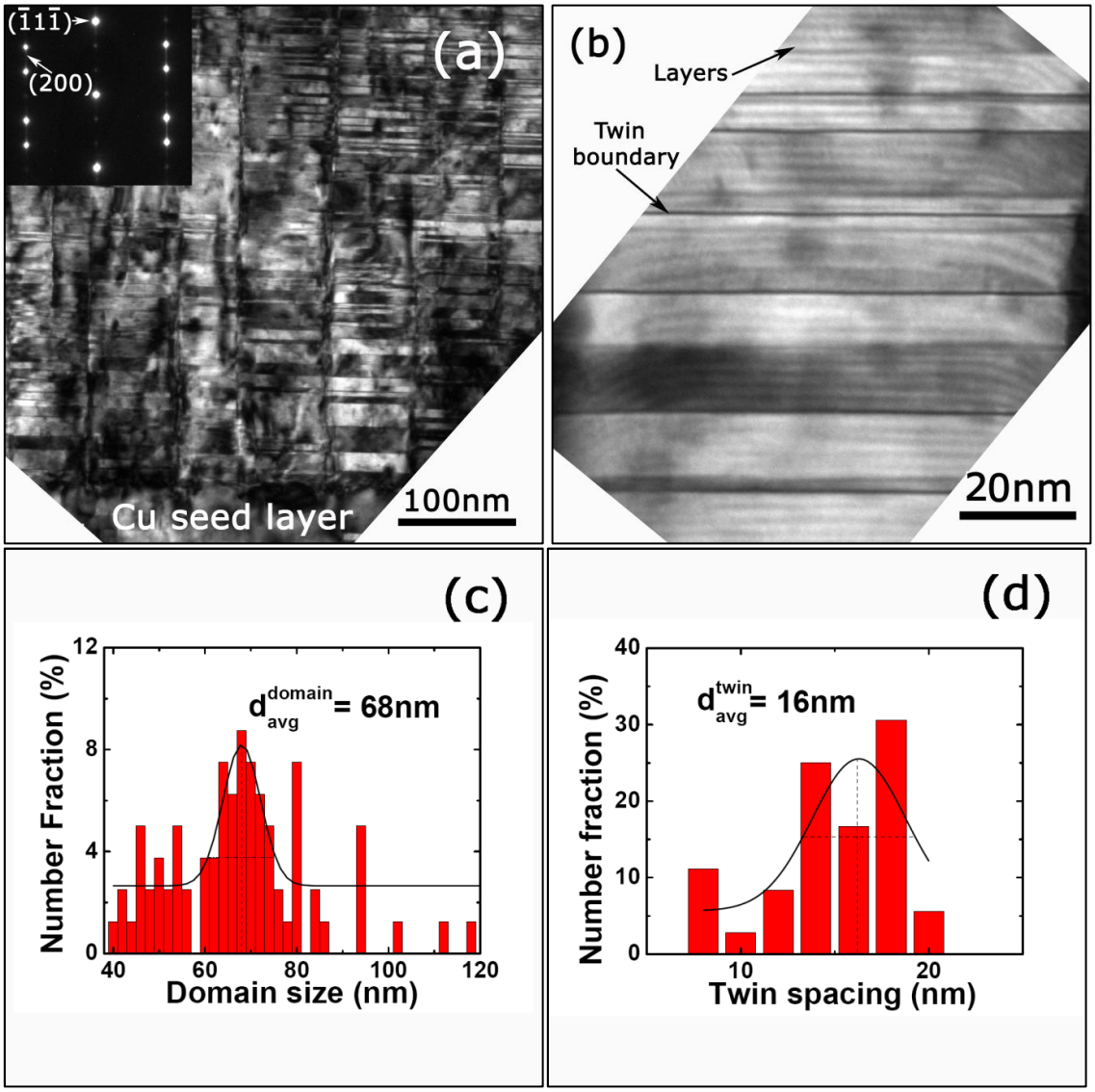

Figure 3.9 Cross-sectional TEM images of as deposited Cu 1nm/ Ni 1nm on Si (110) under (a) low magnification and (b) high magnification. (a) The inserted SAD pattern indicates a strong (111) texture. (b) Nanotwins that penetrate layer interfaces are observed. Statistical distribution of (c) domain size and (d) twin spacing are collected.

3.2 Multilayers hardness

Because Cu/Ni multilayers were deposited on hard Silicon substrate coated with soft Cu seed layer, the multilayers indentation hardness were determined by eliminating substrate [42] and soft seed layer effect when the indentation depth is around 10% of total thickness. Figure 3.10 reveals the measured indentation hardness, H_{IT}, vs. indentation depth of highly textured (111) Cu/Ni 2.5 nm and Cu/Ni 1 nm multilayers. Real multilayer hardness can be determined by eliminating indentation size, soft seed layer, and substrate effects at different indentation depth. At lower indentation depth (75 - 125 nm), the H_{IT} increases due to the indentation size effect. When indentation depth is large (250 - 300 nm), the hard substrate affects the multilayers' indentation hardness. Multilayers hardness results are collected at 125 - 200 nm indentation depth. Hardness has a small drop due to Cu seed layer effect when indentation depth is between 200nm and 250nm.

The hardness of high (100) and (111) textured Cu/Ni multilayers are plotted as a function of $h^{-0.5}$ in Figure 3.11. For comparison, we also show the hardness data of evaporated (100) textured Cu/Ni multilayers [5]. The following distinct features are noticed.

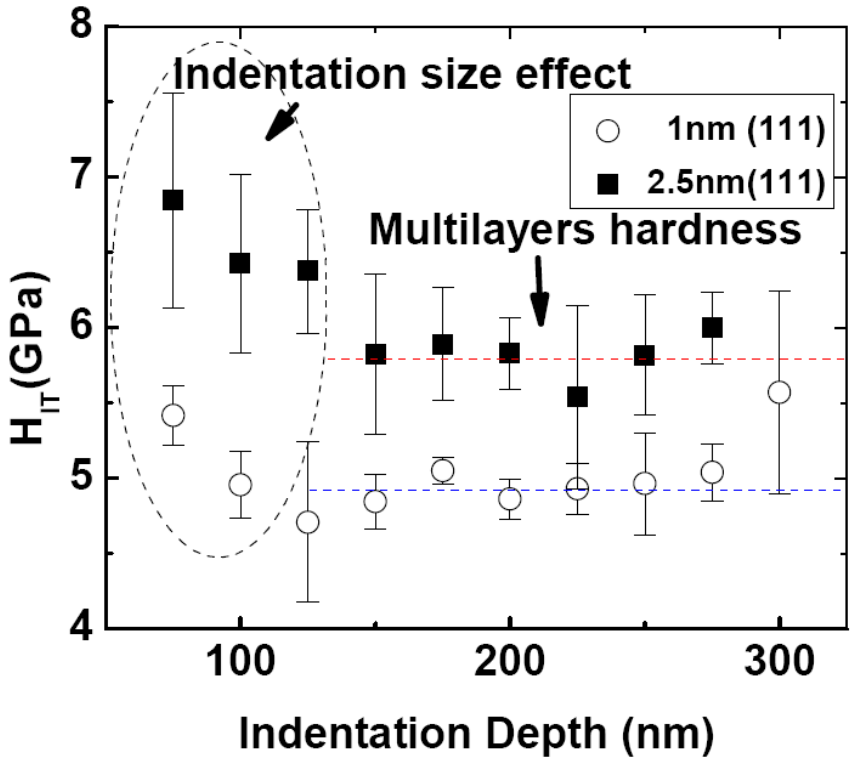

Figure 3.10 Hardness vs. indentation depth of highly textured (111) Cu 2.5nm / Ni 2.5nm and Cu 1nm / Ni 1nm multilayers. Real multilayer hardness can be determined by eliminating indentation size, soft seed layer, and substrate effects.

a. At the same h, in general, the hardnesses of Cu/Ni (111) films are greater than those of Cu/Ni (100) films across all length scales. The evolution of hardnesses of two sets of Cu/Ni (100) studies with $h^{-0.5}$ agrees with each other.

b. At large layer thickness ($h \geq 50$nm), the Hall-Petch slopes, which were calculated by dividing the hardness by a factor of 3, are almost the same for the three systems, ~ 0.1 MPa/m^2. The hardness of Cu/Ni multilayers with (100) texture approaches that of Cu (100) single crystal films, whereas that of Cu/Ni

(111) textured films is nearly the same comparing to that of epitaxial Cu (111) films. The hardnesses of epitaxial Cu (100), (111) and polycrystal Ni are indicated by horizontal dash lines in the same plot.

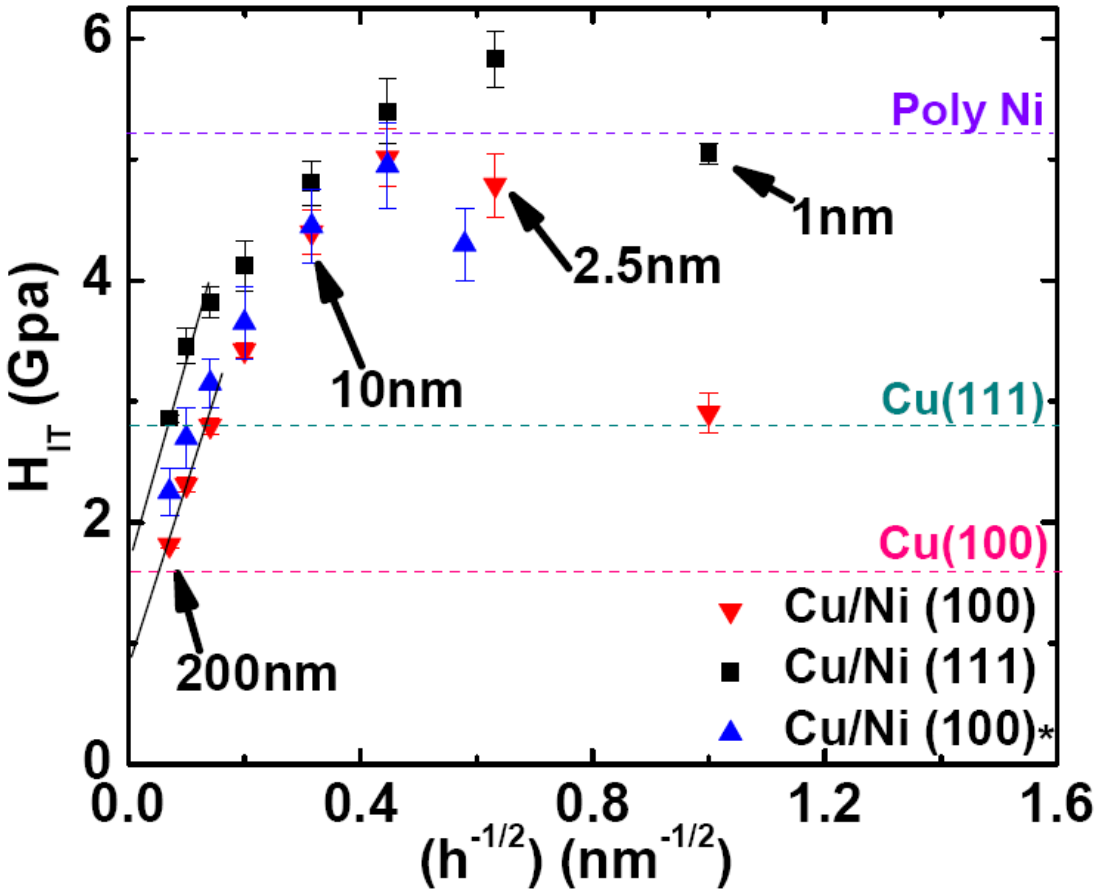

Figure 3.11 Comparison of hardness vs. $h^{-0.5}$ plots for various Cu/Ni multilayer systems, including sputtered highly (111), (100) textured Cu/Ni, and evaporated highly (100) textured Cu/Ni [5-6]. The hardness of evaporated and sputtered (100) textured Cu/Ni are comparable, and reach the highest at h=5nm. The highest hardness of (111) textured Cu/Ni is at h=2.5nm, and higher than single layer Ni hardness.

c. In the range of 50 nm > h > 5 nm, the hardness increases with decreasing layer thickness, but the rate of increases deviates from the linear relation as predicted by the Hall-Petch slope shown as dash lines in all systems.
d. The peak hardness of highly textured (111) films occurs when h = 2.5 nm, greater than the hardness of polycrystalline Ni. The peak hardnesses of sputtered (100) textured Cu/Ni are observed at h of 5 nm in both sputtered and evaporated multilayers.
e. Softening, referring to the decrease of hardness at smaller h, exists in both (111) and (100) textured multilayers. However, softening is significant in Cu/Ni (100) films especially when h is 1 nm, whereas moderate softening is observed in Cu/Ni (111) textured films at the same h.

3.3 Discussion

3.3.1 Evolution of microstructure with layer thickness

Highly textured (100) and (111) Cu/Ni multilayers are obtained on different substrates. At greater h, Cu and Ni (100) (or (111)) peaks are clearly separated indicating that the interface between Cu and Ni is semi-coherent. The coherency improves with decreasing h, due to increasing constraints from layer interface. A single peak with an average d-spacing of Cu and Ni (100) or (111) interplanar spacing is observed at small h, indicating the formation of coherent interface. Furthermore the epitaxial quality of films enhances at smaller h as reflected by greater peak intensity. Microscopy studies reveal that Cu/Ni (100) multilayers with 2.5 nm thickness have

coherent interface with cube-on-cube orientation relationship. This is consistent with previous studies of e-beam evaporated Cu/Ni (100) films with similar layer thickness [5].

3.3.2 Coherent interface and critical layer thickness to form misfit dislocations

The lattice mismatch between Cu and Ni is 2.63% (a_{Cu} = 3.615 Å, a_{Ni} = 3.52 Å). When coherent Cu/Ni interface forms, tensile stress will develop in Ni and compressive stress arise in Cu. With increasing thickness of the individual component, the amount of energy stored elastically in the films is sufficiently high, so that the formation of misfit dislocations will relieve the coherency stress (elastic energy).

The critical thickness to form perfect misfit dislocations in (111) Cu-Ni bilayers can be calculated by[43]

$$h_c = \frac{b}{8\pi(1+\upsilon)f}\left[\ln\left(\frac{h_c}{b}\right) + 1\right] \qquad (3.1)$$

where the magnitude of burgers vector, b, is 0.25 nm, mismatch strain f is 2.3%, Poisson's ratio is 0.3. The calculated h_c is 0.5 nm. This analysis underestimates the critical thickness to form misfit dislocations since, in reality, the Ni is sandwiched between two Cu layers during the deposition of multilayers. The corrected critical thickness in Cu/Ni multilayer should therefore be 2 times that of $h_c$of bilayers, or ~ 1 nm.

3.3.3 The formation of twins in (111) textured Cu/Ni multilayer at smaller h

As illustrated in Chapter I, low γ_t and high deposition rate will enhance the formation of nanoscale twins. However, in the current studies, a similar deposition rate leads to a large difference in twin density in Ni. For instance twins are barely observed in Ni in (111) textured multilayers with h greater than 10 nm. But high density growth twins are observed in Ni when h reduces to 5 nm or less. Hence other mechanisms have to be considered to explain the formation of twins. Here we consider two main possibilities.

a. Twins are formed in Ni to reduce the formation of incoherent twin boundaries in Cu.

As shown in Figure 3.12, an enlarged schematic of (111) textured Cu/Ni multilayers represents the 4 types of twin boundaries in Figure 3.7 (a). “a”, is a coherent twin boundary (CTB) in Cu layer, can be obtained directly due to low SFE of Cu. “b” in epitaxial nanotwinned Cu, is an incoherent twin boundary (ITB)[27,44]. Based on estimation from MD simulations [45], The formation energy of ITB in epitaxial is at least 500mJ/m^2, much larger than energy to form CTB.

When penetrating into the Ni layer, ITB is blocked due to high SFE and high modulus of Ni. A CTB in Ni, “c”, is then formed to release the energy from ITB in Cu. This CTB continues penetrating layer interface to Cu layer, referred to as “d” in Figure 3.12, as following the principle of misfit twins and low formation energy of CTB in Cu.

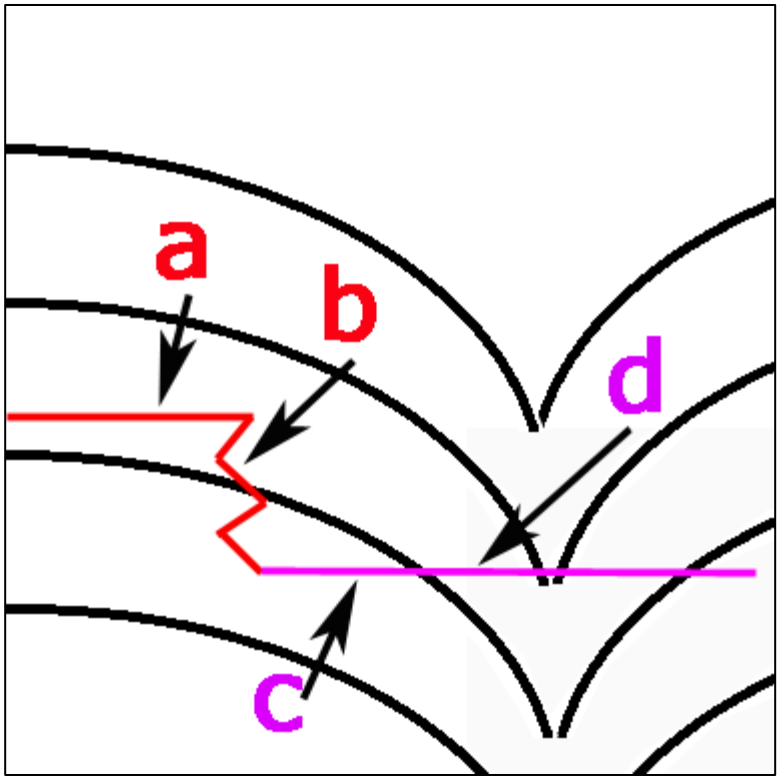

Figure 3.12 A schematic of twin boundaries at in (111) Cu/Ni 2.5nm multilayer.

Compare with an average twin spacing of ~ 10 nm in single layer nanotwinned (111) Cu, the average twin spacing in Cu/Ni 1 nm multilayer is ~ 16 nm under comparable deposition rate [26]. This assumption can explain the existence of high density twins in Ni at h = 2.5 nm, but no existence of twins in Ni at h = 10nm. In Cu/Ni multilayers, ITB could release enough energy in only Cu at large h (ex. 10nm), but not enough at small h (ex. 2.5nm). Therefore, compare with high energy of ITB in Cu, CTB in Ni is more likely to form.

b. Forming misfit twins to alleviate coherency stress

Figure 3.3 reveals a large coherency stress at h = 2.5 nm. The curvature of Cu/Ni multilayers columns continues increase due to the increase of coherency stress. Large coherency stress and bowl structure increase the possibility to form misfit twins in Ni. As illustrated in Chapter I, large coherency will increase $|E_{int,twin/misfit}|$ in Equation 1.10 ($E_f = E_{s,twin} + E_{int,twin/misfit} + \Gamma_t$), then decrease the formation energy to form twins (E_f). Interfaces bowl structure increase the angle φ between twin boundaries and interfaces, then further decrease Γ_t and E_f. This assumption illustrates the existence of nanotwins in Ni at only smaller h and the penetration of twin boundaries. Furthermore, Because of the mismatch strain of Cu/Ni is ~ 2.6%, which is less than 3.8%, the critical thickness to form misfit twins is greater than the critical thickness to form perfect misfit dislocations [30]. Based on previous calculation, the critical thickness of perfect misfit dislocations is ~ 1 nm. Thus, the critical thickness of misfit twinning is larger than ~1 nm, which corresponds to the much less twin spacing at h = 2.5 nm comparing to that at h = 1 nm in Figure 3.7 and Figure 3.9.

3.3.4 Twin interface induced strengthening in Cu/Ni multilayers

In the highly (100) textured Cu/Ni multilayers, only Cu/Ni interface acts as a obstacle to dislocations and the strengthening mechanism has been well studied at different h [11,14,23,46]. However, in the highly (111) textured Cu/Ni multilayers, there are three different planar boundaries that can act as obstacles: Cu/Ni interface, twins in Cu

and twins in Ni. The question is: does twin significantly strengthen the multilayers? If so, at what layer thickness will twin interface start to contribute to the strengthening?

First, we consider the Hall-Petch strengthening at large layer thickness (h ≥ 50nm), the Hall-Petch slopes are 0.097MPa/m^2, and 0.0.077MPa/m^2, in (111) texture and evaporate (100) texture, respectively. The Hall-Petch slope (K_{HP}) is typically expressed as [6]:

$$K_{HP} = \sqrt{\frac{\tau^* \mu b}{\pi(1-\upsilon)}} \qquad (3.2)$$

where $\tau^*$is the critical interface barrier shear stress, μ is the shear modulus (μ is about 48GPa for Cu), b is the Burgers vector (0.25 for Cu), and υ is Poisson's ratio (≈0.3). We obtain $\tau^* \approx$ 1.72 GPa for (111) textured Cu/Ni multilayers with twins in Cu, which corresponds to Rao and Hazzledine [23] estimated $\tau^* \approx 0.03\text{-}0.04\mu$ (τ^*= 1.44-1.92GPa for Cu) by MD simulation. Since there is no twin boundary in Ni at large layer thickness, there is no twin strengthening in Ni. Also the shear stress is less than 1.8 GPa [47] (Hoagland estimated by MD simulation), which is a required shear stress to transmit a dislocation across a twin boundary in Ni. This indicates that twin boundaries in Cu alone could not contribute to strengthening at Hall-Petch regime.

Second, when h < 50 nm, the dislocation pile-ups do not form against interfaces, and the single dislocation bowing via Orowan type of mechanism starts to contribute to the deformation within the layer. An upper bound of this interface barrier stress is $\tau^* \approx$ 0.8 GPa as estimated from the H-P slope in Cu [6]. In (111) textured Cu/Ni multilayers at h = 10 nm, the critical resolved shear stress in Cu by applying CLS model (equation 1.3) is 0.7 GPa. Same as in Hall-Petch regime, the resolved shear stress is larger to

transmit a dislocation across twin boundary in Cu, but smaller to transmit in Ni. Since no twin boundaries existence in Ni at this range, twin boundaries in Cu alone could not contribute to extra strengthening on top of layer interface in a regime where CLS mechanism operates.

Third, when h is less than 10nm, the critical resolved shear stress is larger than 0.8 GPa, and a single dislocation starts transmission across interface. Koehler stress, misfit dislocation, and coherency stress starts contributing to the interface barrier resistance. The shear stress is 0.863GPa by applying equation 1.6 ($\tau = bRG\sin\theta/4\pi h$). Since twin boundaries in Ni begin to form at this range, they block the transmission of dislocations since the applied shear stress is less than critical shear stress (1.8GPa) to transmit across twin interface in Ni. Figure 3.11 confirms this assumption, the hardness of (111) texture Cu/Ni is much harder than (100) texture when h is less than 10nm. Especially when h = 2.5 nm, the hardness continues to increase in (111) textured films, whereas softening occurs in (100) texture. Twin interface induced strengthening in this range is evident.

The softening in (100) texture at h below 5 nm can be interpreted based on two principles. First, we will consider the critical thickness, h_t, below which interface remain transparent, i.e. no dislocation pile up at the interfaces. The calculated h_t for Cu/Ni multilayer is ~ 7.5 nm by applying equation 1.7 ($h_t = \frac{bn}{(1+\upsilon)\epsilon_m}$). This corresponds to the h with the highest hardness (5nm). Intermixing between Cu and Ni is another reason that may lead to softening. Due to the high possibility to form solid solution in Cu and Ni, interface intermixing is likely to occur which may be significant when h is a

few nm or less. And hence the resistance of interface to the transmission of dislocation is considerably reduced. There is also intermixing effect in (111) Cu/Ni multilayer. However, due to the twins in Cu/Ni at smaller h, the hardness continues to increase at h = 2.5 nm. And the softening in Cu/Ni 1 nm films with (111) texture is much less than that in (100) textured Cu/Ni 1 nm multilayers.

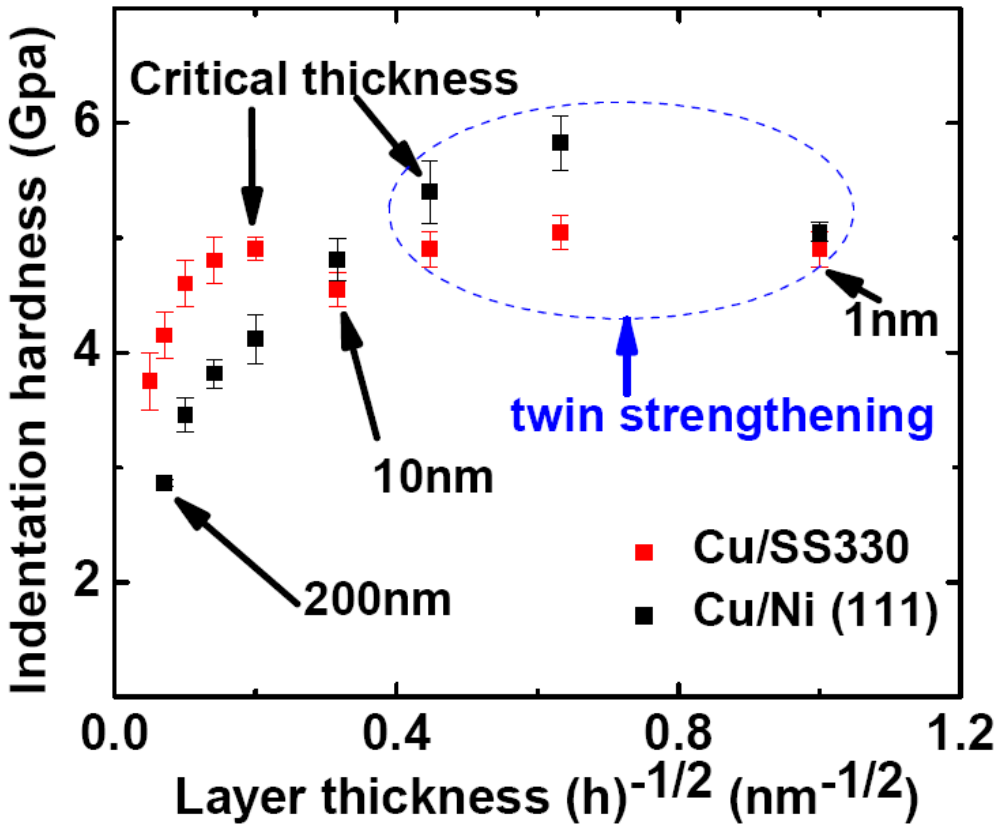

Figure 3.13 Comparison of hardness vs. $h^{-0.5}$ plots for two multilayer systems with nanotwins, including highly (111) textured Cu/Ni, and Cu /330 Stain Steel (SS)[6]. Nanotwins contribute the hardness at h<10nm. This is related to the critical thickness of not forming dislocation pile ups at interfaces.

Therefore, at smaller h, Cu/Ni multilayer without twins exhibits more dramatic softening, and reaches about rule of mixture hardness of Cu and Ni. However, the hardness of Cu/Ni multilayer with twin interfaces remains significantly higher than rule-of-mixture composite. Softening in (111) textured multilayer is closely related to the decrease in twin density. This phenomenon is also shown in Cu/330 stainless steel (SS) in Figure 3.13, due to low lattice mismatch (0.92%), the hardness reach the highest at around the critical thickness (h_t = 20.7 nm). However, twins in Cu and 330SS also contribute to strengthening below the critical thickness.

CHAPTER IV

SUMMARY AND CONCLUSION

In this thesis, Sputtered, highly (111) and (100) textured Cu/Ni multilayers with individual layer thickness, h, varying from 1 to 200 nm. At greater h, XRD patterns of Cu and Ni (100) (or (111)) peaks are clearly separated indicating that the interface between Cu and Ni is semi-coherent. When h decreases to 5 nm or less, XRD spectra show significant peak distortions due to coherency stress. High resolution microscopy studies confirm the coexistence of nanotwins and coherent layer interfaces in highly (111) textured Cu/Ni mutilayers. Nanoscale twins can be formed in Cu at all h and in Ni at smaller h. Multilayer hardnesses increase with decreasing h, approach maxima at h of 2.5-5 nm, and show softening thereafter.

In this thesis, a detail comparison between (111) and (100) textured Cu/Ni is made in both microstructure and strengthening. The influences of both coherent layer interfaces and twin interfaces on strengthening mechanisms are discussed. In this study, the possible mechanisms to form high density growth twins in Ni are discussed.

REFERENCES

1 M. N. Baibich, J. M. Broto, A. Fert, F. Nguyen, F. Petroff, P. Etienne, G. Creuzet, A. Friederich, and J. Chazelas, "Giant magnetoresistance of (001)Fe/(001)Cr magnetic superlattices," Physical Review Letters **61** (21), 2472 (1988).

2 P. Grünberg, R. Schreiber, Y. Pang, M. B. Brodsky, and H. Sowers, "Layered magnetic structures: evidence for antiferromagnetic coupling of Fe layers across Cr interlayers," Physical Review Letters **57** (19), 2442 (1986).

3 K. P. Jayadevan and T. Y. Tseng, "Review composite and multilayer ferroelectric thin films: Processing, properties and applications," Journal of Materials Science: Materials in Electronics **13**, 439 (2002).

4 E. G. Fu, J. Carter, G. Swadener, A. Misra, L. Shao, H. Wang, and X. Zhang, "Size dependent enhancement of helium ion irradiation tolerance in sputtered Cu/V nanolaminates," Journal of Nuclear Materials **385,** 629 (2009).

5 A. Misra, M. Verdier, Y. C. Lu, H. Kung, T. E. Mitchell, M. Nastasi, and J. D. Embury, "Structure and mechanical properties of Cu-X (X = Nb,Cr,Ni) nanolayered composites," Scripta Materialia **39,** 555 (1998).

6 X. Zhang, A. Misra, H. Wang, T. D. Shen, M. Nastasi, T. E. Mitchell, J. P. Hirth, R. G. Hoagland, and J. D. Embury, "Enhanced hardening in Cu/330 stainless steel multilayers by nanoscale twinning," Acta Materialia **52,** 995 (2004).

7 E. G. Fu, N. Li, A. Misra, R. G. Hoagland, H. Wang, and X. Zhang, "Mechanical properties of sputtered Cu/V and Al/Nb multilayer films," Materials Science and Engineering A **493**, 283 (2008).

8 J. McKeown, A. Misra, H. Kung, R. G. Hoagland, and M. Nastasi, "Microstructures and strength of nanoscale Cu-Ag multilayers," Scripta Materialia **46,** 593 (2002).

9 S. P. Wen, R. L. Zong, F. Zeng, Y. Gao, and F. Pan, "Evaluating modulus and hardness enhancement in evaporated Cu/W multilayers," Acta Materialia **55,** 345 (2007).

10 B. J. Daniels, W. D. Nix, and B. M. Clemens, "Enhanced mechanical hardness in compositionally modulated Fe(001)/Pt(001) and Fe(001)/Cr(001) epitaxial thin films," Thin Solid Films **253**, 218 (1994).

11 A. Misra, J. P. Hirth, and H. Kung, "Single-dislocation-based strengthening mechanisms in nanoscale metallic multilayers," Philosophical Magazine A **82**, 2935 (2002).

12 A. Misra, M. J. Demkowicz, J. Wang, and R. G. Hoagland, "The multiscale modeling of plastic deformation in metallic nanolayered composites," Journal of Materials **60,** 39 (2008).

13 J. R. Weertman, "Hall-Petch strengthening in nanocrystalline metals," Materials Science and Engineering: A **166 (**1-2), 161 (1993).

14 P. M. Anderson and C. Li, "Hall-Petch relations for multilayered materials," Nanostructured Materials **5**, 349 (1995).

15 P. M. Anderson and J. S. Carpenter, "Estimates of interfacial properties in Cu/Ni multilayer thin films using hardness data," Scripta Materialia **62,** 325 (2010).

16 H. W. Liu and Q. Gao, "Equivalence between dislocation pile-ups and cracks," Theoretical and Applied Fracture Mechanics **12,** 195 (1990).

17 J. D. Embury and J. P. Hirth, "On dislocation storage and the mechanical response of fine scale microstructures," Acta Metallurgica et Materialia **42,** 2051 (1994);

18 M. A. Phillips, B. M. Clemens, and W. D. Nix, "A model for dislocation behavior during deformation of Al/Al3Sc (fcc/L12) metallic multilayers," Acta Materialia **51**, 3157 (2003).

19 A. Misra, J. P. Hirth, and R. G. Hoagland, "Length-scale-dependent deformation mechanisms in incoherent metallic multilayered composites," Acta Materialia **53**, 4817 (2005).

20 M. J. Demkowicz, J. Wang, and R. G. Hoagland, "Interfaces between dissimilar c rystalline solids," in Dislocations in Solids, Elsevier **14,** 141 (2008).

21 R. G. Hoagland, R. J. Kurtz, and C. H. Henager, Jr. "Slip resistance of interfaces and the strength of metallic multilayer composites," Scripta Materialia **50,** 775 (2004).

22 J. S. Koehler, "Attempt to design a strong solid," Physical Review B **2** (2), 547 (1970).

23 S. I. Rao and P. M. Hazzledine, "Atomistic simulations of dislocation-interface interactions in the Cu-Ni multilayer system," Philosophical Magazine A, **80**, 2011 (2000).

24 O. Anderoglu, A. Misra, J. Wang, R. G. Hoagland, J. P. Hirth, and X. Zhang, "Plastic flow stability of nanotwinned Cu foils," International Journal of Plasticity **26,** 875 (2010).

25 L. Lu, Y. Shen, X. Chen, L. Qian, and K. Lu, "Ultrahigh strength and high electrical conductivity in copper," Science **304,** 422 (2004).

26 O. Anderoglu, A. Misra, F. Ronning, H. Wang, and X. Zhang, "Significant enhancement of the strength-to-resistivity ratio by nanotwins in epitaxial Cu films," Journal of Applied Physics **106** (2), 024313 (2009).

27 O. Anderoglu, A. Misra, H. Wang, F. Ronning, M. F. Hundley, and X. Zhang, "Epitaxial nanotwinned Cu films with high strength and high conductivity," Applied Physics Letters **93** (8), 083108-1-3 (2008).

28 O. Anderoglu, A. Misra, H. Wang, and X. Zhang, "Thermal stability of sputtered Cu films with nanoscale growth twins," Journal of Applied Physics **103**, 094322 (2008).

29 Y. Zhang, L. Liu, and T. Y. Zhang, "Strain relaxation in heteroepitaxial films by misfit twinning: II. Equilibrium morphology," Journal of Applied Physics **101** (6), 63502-1-13 (2007).

30 L. Liu, Y. Zhang, and T. Y. Zhang, "Strain relaxation in heteroepitaxial films by misfit twinning. I. Critical thickness," Journal of Applied Physics **101** (6), 63501-1-12 (2007).

31 A. Misra, M. Verdier, H. Kung, J. D. Embury, and J. P. Hirth, "Deformation mechanism maps for polycrystalline metallic multilayers," Scripta Materialia **41,** 973 (1999).

32 ISO 14577-12002, Metallic materials - Instrumented indentation test for hardness and materials parameters, International Standard.

33 N. Panich and Y. Sun, "Effect of penetration depth on indentation response of soft coatings on hard substrates: a finite element analysis," Surface Coating Technology **182** (2-3), 342 (2004).

34 W. L. Bragg, "The diffraction of short electromagnetic waves by a crystal," Proceedings of the Cambridge Philosophical Society **17,** 43 (1913).

35 E. E. Fullerton, I. K. Schuller, H. Vanderstraeten, and Y. Bruynseraede, "Structural refinement of superlattices from x-ray diffraction," Physical Review **B** 45 (16), 9292 (1992).

36 I. K. Schuller, "New class of layered materials," Physical Review Letters **44** (24), 1597 (1980).

37 D. B. Williams and C. B. Carter, Transmission Electron Microscopy: A Textbook for Materials Science. Plenum Press, New York (1996).

38 S. P. Baker and N. Burnham, Symposium Q: Fundamentals of Nanoindentation and Nanotribology, MRS Fall Meeting Tutorial Program, Boston, MA (2000).

39 W. C. Oliver and G. M. Pharr, "An improved technique for determining hardness and elastic modulus using load and displacement sensing indentation experiments," Journal of Materials Research **7,** 1564 (1992).

40 J. B. Pethica and W. C. Oliver, "Mechanical properties of nanometre volumes of material: use of the elastic response of small area indentations," Thin Films: Stresses and Mechanical Properties Symposium, 13 (1989).

41 T. J. Bell, J. S. Field, and M. V. Swain, "Precision hardness & elastic modulus measurements of thin films & cross-sections," Materials Forum **17** (2), 127 (1993).

42 R. Saha and W. D. Nix, "Effects of the substrate on the determination of thin film mechanical properties by nanoindentation," Acta Materialia **50**, 23 (2002).

43 R. Hull and J. C. Bean, "Misfit dislocations in lattice-mismatched epitaxial films," Critical Reviews in Solid State and Materials Sciences **17** (6), 507 (1992).

44 J. Wang, O. Anderoglu, J. P. Hirth, A. Misra, and X. Zhang, "Dislocation structures of 3 {112} twin boundaries in face centered cubic metals," Applied Physics Letters **95** (2), 021908 (2009).

45 J. Wang, N. Li, O. Anderoglu, X. Zhang, A. Misra, J. Y. Huang, and J. P. Hirth, "Detwinning mechanisms for growth twins in face-centered cubic metals," Acta Materialia **58**, 2262 (2010).

46 P. M. Anderson, T. Foecke, and P. M. Hazzledine, "Dislocation-based deformation mechanisms in metallic nanolaminates," MRS Bulletin **24**, 27 (1999).

47 R. G. Hoagland, T. E. Mitchell, J. P. Hirth, and H. Kung, "On the strengthening effects of interfaces in multilayer fcc metallic composites," Philosophical Magazine A **82**, 643 (2002).

VITA

Name:	Yue Liu
Address:	Department of Mechanical Engineering c/o Dr. Xinghang Zhang Texas A&M University College Station, TX 77843-3123
Email Address:	Liu.y0203@gmail.com
Education:	B. S., Microelectronics, Fudan University, China, 2008 M. S., Mechanical Engineering, Texas A&M University, College Station, TX, USA, 2010